BNL-72286-2002

The Center for Data Intensive Computing

in affiliation with the Departments of

Computer Science and
Applied Mathematics and Statistics
State University of New York at Stony Brook

www.bnl.gov/cdic

James Glimm, Director

November 2002

Brookhaven National Laboratory
P.O. Box 5000
Upton, NY 11973-5000
www.bnl.gov

Managed by
Brookhaven Science Associates, LLC
for the United States Department of Energy under
Contract No. DE-AC02-98CH10886

DISCLAIMER

This report was prepared as an account of work sponsored by an agency of the United States Government. Neither the United States Government nor any agency thereof, nor any of their employees, nor any of their contractors, subcontractors, or their employees, makes any warranty, express or implied, or assumes any legal liability or responsibility for the accuracy, completeness, or any third party's use or the results of such use of any information, apparatus, product, or process disclosed, or represents that its use would not infringe privately owned rights. Reference herein to any specific commercial product, process, or service by trade name, trademark, manufacturer, or otherwise, does not necessarily constitute or imply its endorsement, recommendation, or favoring by the United States Government or any agency thereof or its contractors or subcontractors. The views and opinions of authors expressed herein do not necessarily state or reflect those of the United States Government or any agency thereof.

FOR UNCLASSIFIED, UNLIMITED STI PRODUCTS

Available electronically at:

OSTI:
http://www.osti.gov/bridge

Available for a processing fee to U.S. Department of Energy and its contractors, in paper from:

U.S. Department of Energy
Office of Scientific and Technical Information
P.O. Box 62
Oak Ridge, TN 37831
Phone: (865) 576-8401
Facsimile: (865) 576-5728
E-mail: reports@adonis.osti.gov

National Technical Information Service (NTIS):

Available for sale to the public from:

U.S. Department of Commerce
National Technical Information Service
5285 Port Royal Road
Springfield, VA 22131
Phone: (800) 553-6847
Facsimile: (703) 605-6900
Online ordering: http://www.ntis.gov/ordering.htm

CENTER FOR DATA INTENSIVE COMPUTING

Page

1. Mission....3

2. Overview....3

3. Personnel....4

4. Research....7

4.1 SciDAC: TSTT at CDIC....8

4.2 High Energy and Nuclear Physics....8
- 4.2.1 Muon Collider Target....9
- 4.2.2 Accelerator Design....12
- 4.2.3 High Intensity Beam Simulation Project....17
- 4.2.4 MiniBooNe Detector Analysis....18

4.3 Basic Energy Sciences....20
- 4.3.1 TSTT: Atomization and Spray....21
- 4.3.2 Quantum Monte Carlo Simulations of Magnetic Systems....24
- 4.3.3 Magnetic Nanowires....27
- 4.3.4 Superconductivity....28
- 4.3.5 Molecular Dynamics on the QCDOC....30
- 4.3.6 Uranium Equation of State....31
- 4.3.7 Numerical Simulation of Photonic Devices....34

4.4 Biological and Environmental Research....36
- 4.4.1 Parallel Implementation of an Atmospheric Aerosol Model....36
- 4.4.2 Neuron Imaging....37
- 4.4.3 Cardiac Electrophysiology....39

4.5 Advanced Scientific Computing....40
- 4.5.1 TSTT: Frontier-Lite....41
- 4.5.2 Magnetohydrodynamics of Multifluid Systems....43
- 4.5.3 ViStA: Visual Statistical Analyzer....47
- 4.5.4 Uncertainty Quantification....53
- 4.5.5 Visualization....55
- 4.5.6 Cluster Computing....56

1. MISSION

CDIC was established to provide state-of-the-art computational and computer science for the Laboratory and for the broader DOE and scientific community.

We achieve this goal by performing advanced scientific computing research in the Laboratory's mission areas of High Energy and Nuclear Physics, Biological and Environmental Research, and Basic Energy Sciences. We also assist other groups at the Laboratory to reach new levels of achievement in computing.

We are "data intensive" because the production and manipulation of large quantities of data are hallmarks of scientific research in the 21st century and are intrinsic features of major programs at Brookhaven.

An integral part of our activity to accomplish this mission is a close collaboration with the University at Stony Brook.

2. OVERVIEW

Modern science is critically dependent on computers and computing. A mix of capabilities is required, which range from advanced hardware to high level and focused software efforts to high speed networking - all aimed at the solution of forefront scientific problems which are consistent with our missions in High Energy and Nuclear Physics, Biology and Medicine, Materials and Chemical Sciences, Energy, Environmental Science, and National Security.

National plans for Information Technology in the early 21st century call for computing at the level of 100 teraflops and data storage in the petabytes. However, because this computational power will be obtained from massively parallel architectures, there is no guarantee that scientific and engineering codes will actually achieve these speeds. This issue is central to the Department of Energy's five-year program "Scientific Discovery Through Advanced Scientific Computing" (SciDAC). It is central to planned large-scale development of parallel nodes, each with high-speed vector processing. CDIC plays a prominent role in the SciDAC program through TSTT - Terascale Simulation Tools and Technologies. TSTT is a multi institutional effort to develop interoperable adaptive grid and meshing tools for a wide variety of scientific problems. Targeted applications include accelerator design, fusion, and fluid dynamics. In addition, large-scale computational physics codes aimed at studying the fundamental properties of quarks and gluons (lattice quantum chromodynamics) are planned to run at tens of teraflops.

Requirements for storage of experimental and observational data will reach hundreds of petabytes. Examples at BNL include RHIC, the Relativistic Heavy Ion Collider; US-ATLAS, one of the detectors planned for the Large Hadron Collider at CERN; climate modeling and simulation; brain imaging; protein structure and function; and computational fluid dynamics.

To be useful, this data must be processed, visualized, analyzed, and understood, as well as stored. Ultimately, data achieves value through its influence on some human decision. Increasingly,

decisions will be made on a computer-assisted basis. For this reason, the modern theory of data management goes beyond sheer volume to data intelligence.

CDIC will mount a research program in computational science to develop fundamentally new approaches to the management of large-scale, highly complex data and to assess uncertainties inherent in their use.

CDIC is closely linked with the Department of Applied Mathematics and Statistics and with the Computer Science Department at SUNY Stony Brook, as well as with the Information Technology Division at BNL. The Center Director and one of the staff members hold joint appointments, nine other faculty are CDIC Affiliates, and 10 graduate students contribute to CDIC projects. This arrangement adds critical strength to the Center.

Research in these areas provides a close link to Brookhaven's scientific programs. The Center will promote excellence, Laboratory wide, in scientific computing. CDIC will contribute to progress and productivity at BNL in a broad sense with special emphasis on:

- **High Energy and Nuclear Physics**
- **Biological and Environmental Science**
- **Basic Energy Sciences**
- **Advanced Scientific Computing**

3. PERSONNEL

The Director of the Center for Data Intensive Computing (CDIC) is James Glimm;
James Davenport is the Associate Director, and the Staff Assistant is Claire Lamberti. CDIC is located in Building 463, Room 255, at Brookhaven National Laboratory, Upton NY 11973-5000.

CDIC, established in 1999, presently has a staff of eight, which is expected to approximately double over the next four years. Recruitment of additional new faculty at SUNY Stony Brook, who will be associated with the Center and may hold joint appointments in the Center, will take place over the same time frame. As part of an active, ongoing collaboration with graduate students from Stony Brook, ten Ph.D. students and several undergraduates hold scientific positions in CDIC.

TABLE 1. CDIC STAFF

Name	Position	Phone/email
James Glimm	Director	631-344-8155 (voice) 631-344-5751 (fax) glimm@bnl.gov
James Davenport	Associate Director	631-344-3789 (voice) 631-344-5751 (fax) jdaven@bnl.gov
Wonho Oh	Assistant Scientist	631-344-8156 (voice) 631-344-5751 (fax) woh@bnl.gov

Roman Samulyak	Assistant Scientist	631-344-3304 (voice) 631-344-5751 (fax) rosamu@bnl.gov
Yarema Prykarpatskyy	Research Associate	631-344-8603 (voice) 631-344-5751 (fax) yarpry@bnl.gov
Myoung-Nyoun Kim	Research Associate	631-344-2089 (voice) 631-344-5751 (fax) mnkim@bnl.gov
Isabel Campos	Research Associate	631-344-3051 (voice) 631-344-5751 (fax)
Matej Komelj	Visiting Scientist	631-344-3051 (voice) 631-344-5751 (fax)
Nicholas D'Imperio	Physics Associate	631-344-8589 (voice) 631-344-5751 (fax) dimperio@bnl.gov
Claire Lamberti	Staff Assistant	631-344-3051 (voice) 631-344-5751 (fax) lamberti@bnl.gov

TABLE 2. CDIC AFFILIATES

Name	**Affiliation**	**Expertise**
Carl Anderson	BNL/Biology	Protein Structures
Carmen Benkovitz	BNL/Environmental Sciences	Atmospheric Transport
Michael Creutz	BNL/Physics	Lattice Gauge Theory
Yuefan Deng	SB/Applied Math. & Statistics	Molecular Dynamics
Efstratios Efstathiadis	BNL/ITD	Cluster Computing
Steven Evans	Beth Israel Medical Center	Cardiac Physiology
Flavio Fenton	Hofstra University	Cardiac Simulation
Joanna Fowler	BNL/Chemistry	Medical Imaging
Juliano Franchetti	GSI/Darmstadt	Accelerator Physics
John Grove	Los Alamos National Lab.	Computational Science
Harold Hastings	Hofstra University	Dynamical Systems
Ingo Hoffman	GSI/Darmstadt	Accelerator Physics
Dan Imre	BNL/Environmental Sciences	Mass Spectroscopy
Jiansheng Jiang	BNL/Biology	Protein Structures
Arie Kaufman	SB/Computer Science	Visualization
Xiaolin Li	SB/Applied Math. & Statistics	Computational Science
Brent Lindquist	SB/Applied Math. & Statistics	Porous Media; Image Analysis
Alfredo Luccio	BNL/AGS	Accelerator Design
Edward McFadden	BNL/ITD	Parallel Hardware
Michael McGuigan	BNL/ITD	Visualization & BNCT Simulations
James Muckerman	BNL/Chemistry	Combustion Chemistry

Klaus Mueller	SB/Computer Science	Visualization
Raymond Mugno	SB/Applied Math. & Statistics	Statistics
Hong Qin	SB/Computer Science	Parallel Computing
Arnold Peskin	BNL/CDIC & ITD	Visualization
John Pinezich	TST Corporation	Computational Fluid Dynamics
John Reinitz	SB/Applied Math. & Statistics	Computational Biology
Thomas Robertazzi	SB/Electrical & Computer Engineering	Grid Computing
Eunice Santos	Virginia Polytechnic	Computer Science
Stephen Schwartz	BNL/Environmental Sciences	Aerosol and Climate Modeling
David Sharp	Los Alamos National Laboratory	Computational Science
Leonard Slatest	BNL/ITD	Parallel Computing
William Studier	BNL/Biology	Protein Structures
Nora Volkow	BNL/Directorate	Medical Imaging
Michael Weinert	Univ. of Wisconsin/Milwaukee	Condensed Matter Physics
Torre Wenaus	BNL/Physics	High Energy and Nuclear Physics
Wei Zhu	SB/Applied Math. & Statistics	Statistics; Image Analysis

TABLE 3. STUDENT AFFILIATES	
Name	**Affiliation**
Mihail Busu	SB/Applied Mathematics & Statistics mibusu@amirani.ams.sunysb.edu
Seung Yeon Cho	SB/Applied Mathematics & Statistics sycho@ams.sunysb.edu
Erwin George	SB/Applied Mathematics & Statistics egeorge@ams.sunysb.edu
Wei Guo	SB/Applied Mathematics & Statistics wguo@ams.sunysb.edu
Jing Luo	SB/Computer Science jingluo@cs.sunysb.edu
AndrJa Marchese	SB/Applied Mathematics & Statistics marchese@ams.sunysb.edu
Vito Mirinavicius	SB/Applied Mathematics & Statistics vmirinav@galaxy.ams.sunysb.edu
Natasa Stojic	SB/Physics nstojic@grad.physics.sunysb.edu
Haibin Su	SB/Material Science and Engineering Hsbsu@sun2.bnl.gov
Christina Weaver	SB/Applied Mathematics & Statistics cweaver@ams.sunysb.edu
Tom Welsh	SB/Computer Science tfwelsh@cs.sunysb.edu

4. RESEARCH

CDIC Budget FY 2003
Total: $1,298K

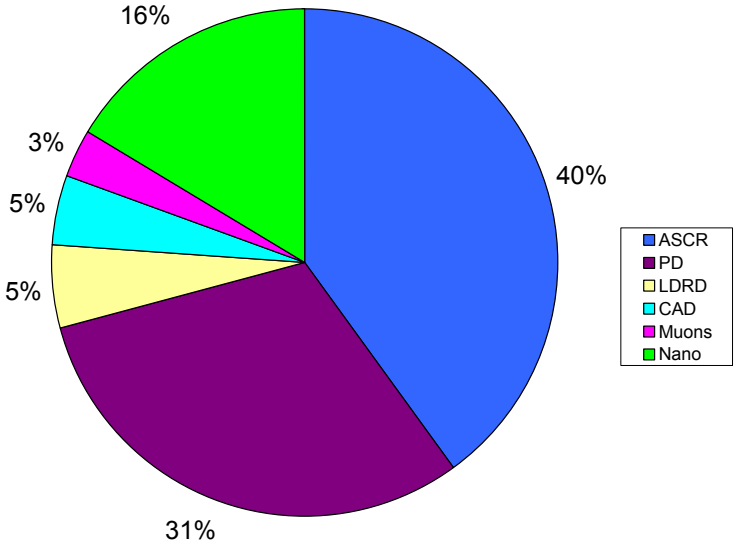

CDIC Projects

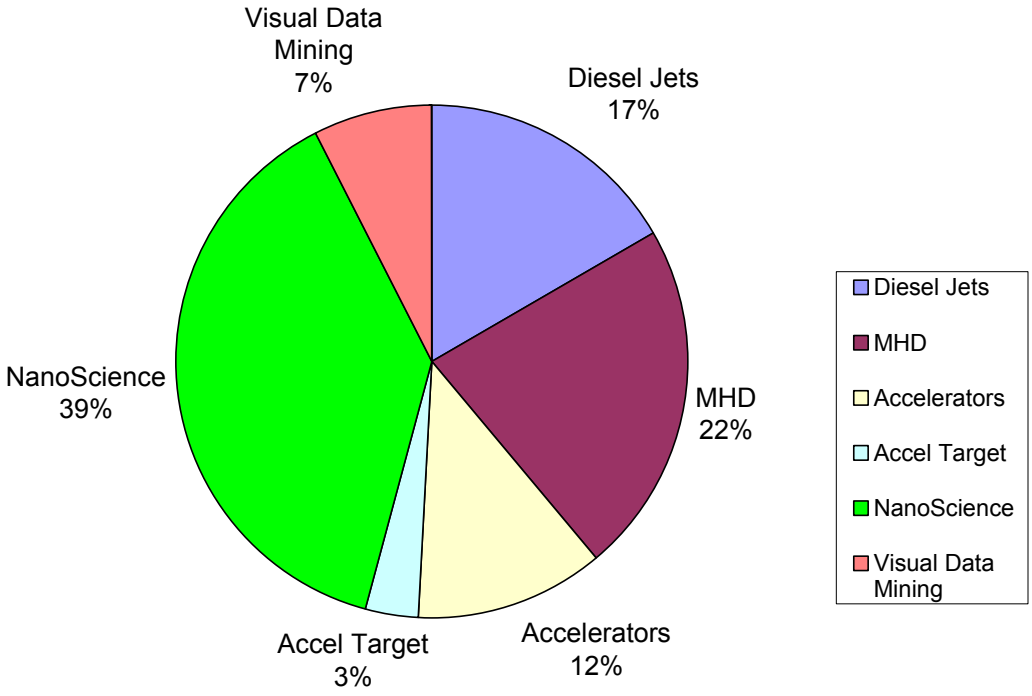

4.1 SciDAC: TSTT at CDIC

Scientific Discovery through Advanced Computing (SciDAC) is a five-year program to develop the Scientific Computing Software and Hardware Infrastructure to support terascale computations for DOE's research programs.

At Brookhaven we have formed an alliance with researchers at Argonne, Livermore, Oak Ridge, Pacific Northwest, Rensselaer, Sandia, and Stony Brook, to develop technologies that enable scientists to use complex mesh and discretization strategies easily, within a single simulation on terascale computers. The Terascale Simulation Tools and Technologies (TSTT) Center will provide interoperable tools to facilitate use of advanced mesh and discretization technologies. The Center will develop standardized interfaces to local mesh refinement and adaptive higher order discretization codes. Existing codes of the Center partners and new codes will be supported to create a plug and play capability, whereby an application user can experiment easily with alternative technologies. Insertion of these tools into targeted applications is part of the Center work plan.

CDIC work within TSTT currently focuses on jet breakup, spray formation, and accelerator applications, and on finite element and front tracking contributions to TSTT technology.

4.2 High Energy and Nuclear Physics

New major physics facilities are central to the vitality of the nation's HENP programs. Due to their expense and complexity, simulation codes are integral to the design process. Design errors have been a major contributor to past instances of project cancellations and missed target performance. For this reason, design teams will increasingly use high performance computing, developed in national, multi-laboratory collaborations to address simulation issues in the design, operation, and control of accelerators.

See Table 4 for a list of current CDIC projects.

TABLE 4. HIGH ENERGY AND NUCLEAR PHYSICS PROJECTS

Project Title	Key Personnel	Comments
Muon Collider Target	R. Samulyak, W. Oh, J. Glimm,	Simulation of the Muon Collider Target
Accelerator Design	R. Samulyak	Parallelization of Design, Control, and Optimization Codes
High-Intensity Beam Simulation Project	I. Hofmann, G. Franchetti	High Current Accelerator Studies
MiniBooNE Detector Analysis	R. Samulyak	Shock Wave Induced PMT Failure

4.2.1 Muon Collider Target

Introduction: Muon Collider. In order to understand the fundamental structure of matter and energy, an advance in the energy frontier of particle accelerators is required. The majority of contemporary high-energy physics experiments utilize colliders. The aim of the multi institutional research group Muon Collider/Neutrino Factory Collaboration is to explore the feasibility of a high energy, high luminosity muon-muon collider. For more information visit the home pages of the Muon Collider Group (http://www.cap.bnl.gov/mumu/mu_home_page.html) and the Center For Accelerator Physics (http://www.nsls.bnl.gov/AccTest/capfiles/CAP.html). The muon collider offers the advantages of greatly increased particle energies over traditional electron-positron (linear) colliders. However, several challenging technological problems remain to be solved. One of the most important is to create an effective target able to generate the high-flux muon beam. The need to operate high atomic number material targets in particle accelerators that will be able to withstand intense thermal shock has led to the exploration of free liquid jets as potential target candidates for the proposed muon collider. The target will be designed as a pulsed jet of mercury (high Z-liquid) interacting in a strong magnetic field with a high energy proton beam. Numerical studies of the mercury jet behavior under such an energy deposition are the main goal of the present research.

Muon Collider Target Design. The proposed target for the Muon Collider is shown schematically in Figure 1. It will contain a series of mercury jet pulses of about 1 cm in diameter and 30 cm in length. Each pulse will be shot at a velocity of 30-35 m/s into a 20 Tesla magnetic field at a small angle to the axis of the magnetic field. When the jet reaches the center of the magnet it will be hit with a 2 ns proton pulse. The proton pulse will deposit about 100 J/g of energy in the mercury.

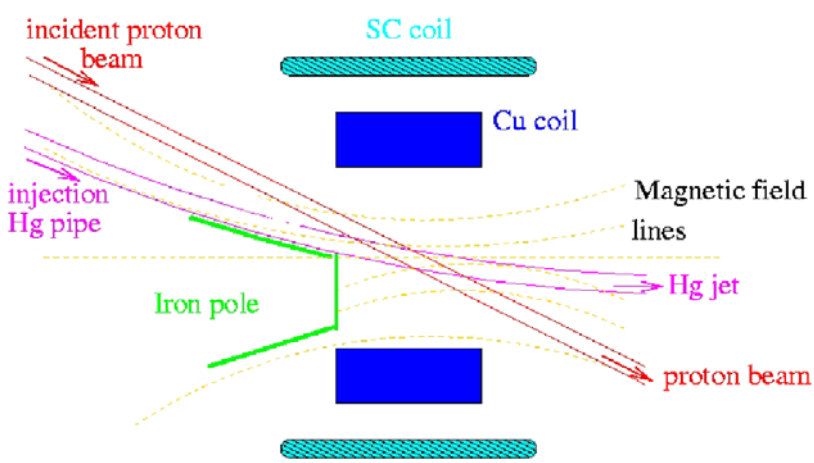

Figure 1. Schematic of the Muon Collider target.

Numerical Simulations. Numerical simulations of the Muon Collider target have been performed using the FronTier-MHD code. The system of MHD equations is a coupled hyperbolic-elliptic system with a geometrically complex moving domain defined by the mercury jet. We have developed a numerical method for solving such systems and the corresponding parallel software. The numerical method treats the MHD system in the operator splitting manner. We use the front

tracking hydro code FronTier with free interface support for solving the hyperbolic subsystem. The elliptic or parabolic part is solved using a mixed finite element method on a grid that conforms dynamically to the moving interface.

The MHD extension of FronTier is described in more detail in Section 4.5.2, Magnetohydrodynamics of Multifluid Systems.

In previous works [3,4], we made some analytical estimates and studied the evolution of conducting liquid jets (and the mercury target in particular) as they enter a strong nonuniform magnetic field. Here we concentrate on the behavior of the target under the influence of the proton beam, and study the Richtmyer-Meshkov type instability induced by shock waves.

In the numerical simulation, the initial mercury jet is taken as a 15 cm long and 1 cm diameter ideal cylinder with no surface perturbations. The influence of the proton pulse was modeled by adding the proton beam energy density to the internal energy density of mercury at a single time step. The distribution of the proton energy deposition in mercury was approximated by a 2d Gaussian distribution. The liquid was modeled using the stiffened polytropic equation of state [5] with the Gruneisen exponent 2.2 and the stiffening constant $P_\infty = 8 \cdot 10^{10}\, g / cm \cdot s^2$. The polytropic gamma law gas was used for the ambient gas. The numerical simulations on a 2100 X 700 grid were performed on 32 processors of a distributed memory cluster of Pentium processors running RedHat Linux. the evolution of the mercury jet due to a single proton pulse energy deposition is depicted in Figure 2.

The external energy deposition in the mercury jet resulted in instantaneous heating and formation of a high pressure domain and a shock wave. A multiple reflection of shock waves from the wall caused a series of surface perturbations that evolved in the form of narrow radial jets. The first jet initialized small, grid-related, surface perturbations. During the later time evolution, neighboring radial jets merged, forming a spatial distribution of RM type surface instabilities independent of the grid size. Due to the interaction of the perturbed interface with the next reflected shock, a period doubling of the surface instabilities was observed during a short period of time. This period doubling was diminished as radial jets merged during the instability growth. Notice that a shock wave reflects from the mercury/gas interface as a rarefaction wave and the result of the rarefaction wave reflection is a shock wave. Therefore a wave propagates twice between the top and bottom jet surfaces before it causes a new set of RM type surface deformations. The multiple reflections of shock/rarefaction waves from the jet surfaces and a series of RM type instabilities on the jet surface were obtained through the use of the stiffened polytropic equation of state to model a single phase fluid. In a forthcoming paper, we will present results of a study of this phenomenon using an equation of state allowing a phase transition (cavitation). It is expected that the mercury will cavitate due to strong rarefaction waves; the cavities will change the dynamics of the interior waves.

Figure 29 of Section 4.5.2 depicts results of the numerical simulation of the Richtmyer-Meshkov type instability evolution in the presence of a strong magnetic field. A uniform magnetic field was applied to the mercury jet along the axis. The Lorentz force due to induced currents reduced both the shock wave speed in the liquid and the velocity of surface instabilities. As a result, surface instabilities were suppressed in a 10 Tesla magnetic field.

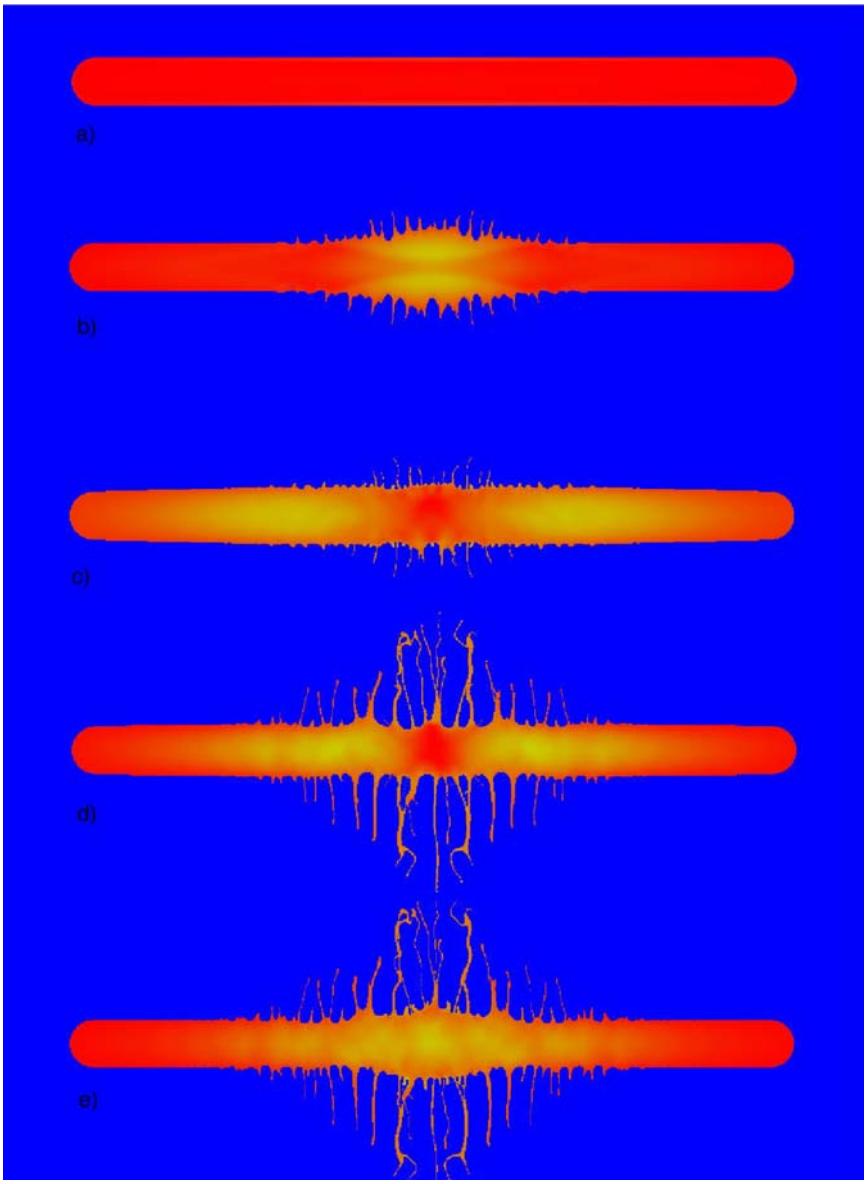

Figure 2. Evolution of the mercury jet due to the proton energy deposition, B = 0:
a) Initial shape of the jet, t = 0; b) Surface instabilities due to the second reflected shock wave, t = 40μs; c) Interaction of the third reflected shock wave with the surface, t = 45μs; d) Surface instabilities due to the third reflected shock wave, t = 59μs; e) Interaction of the fourth reflected shock wave with the surface, t = 67μs.

To model accurately the interaction of the mercury target with proton pulses, a tabulated equation of state for mercury was created in a wide temperature-pressure domain that includes the liquid - vapor phase transition and the critical point. The necessary data describing thermodynamic properties of mercury in such a domain were obtained courtesy of T. Trucano of Sandia National Laboratory. A simplified, two-phase, analytic equation of state containing a liquid-vapor phase transition was also developed assuming an isentropic regime of the flow. In the future, we shall

improve our numerical simulations using the FronTier-MHD code, and both the tabulated and analytic two-phase equations of state.

References

1. Ozaki, S., Palmer, R., Zisman, M., and Gallardo, J., Editors. Feasibility study-II of a muon-based neutrino source. BNL-52623, June 2001; available at http://www.cap.bnl.gov/mumu/studyii/FS2-report.html.
2. Kirk, H., et al. Target studies with BNL E951 at the AGS. *Proc. Particles and Accelerators 2001*, June 18-22, 2001, Chicago, IL.
3. Glimm, J., Kirk, H., Li, X.L., Pinezich, J., Samulyak, R. , and Simos, N. Simulation of 3D fluid jets with application to the Muon Collider target design. In M. Rahman and C. Brebbia, Eds., *Advances of Fluid Mechanics III*, pp. 191-200, WIT Press, 2000.
4. Samulyak, R. Numerical simulation of hydro- and magnetohydrodynamic processes in the Muon Collider target. Lecture Notes in Comp. Sci. **2331**, 391 – 400 (2002).
5. Menikoff, R. and Plohr, B. The Riemann problem for fluid flow of real materials, Rev. Mod. Phys. **61**, 75-130 (1989)

4.2.2 Accelerator Design

Introduction. The SciDAC project Advanced Computing for 21st Century Accelerator Science and Technology is a national research and development effort involving four national laboratories and four universities. The project will develop a comprehensive terascale Accelerator Simulation Environment whose components will enable accelerator physicists and engineers to address a broad range of important issues in next generation accelerator design and operation. These issues, which could not be addressed without terascale resources, range from the high accuracy requirement for modeling complex accelerating structures with tight tolerances to the high resolution requirement needed for the simulation of beam halos in high intensity linear and circular accelerators.

The following target applications are relevant to the BNL accelerator simulation research:

- Simulation of beam dynamics and collective beam instabilities in the BNL AGS and Booster accelerators.
- Simulation of devices for electron cooling.

The CDIC/BNL research goal is to develop algorithms and parallel software libraries for modeling the interaction of particle beams with electromagnetic wake fields in high intensity accelerators, and to model the beam dynamics and beam instabilities in several accelerator facilities. The electromagnetic interaction of an intensive charged particle beam with its vacuum chamber surroundings in an accelerator plays an important role in the beam dynamics and collective beam instabilities. Wake fields, generated by a moving particle in the accelerator pipe and objects such as RF cavities, bellows, stripline monitors etc., affect the motion of all particles in the tail part of the beam. This effect is usually of the same order of magnitude as the space charge effect. While the space charge forces approach zero in the ultrarelativistic limit, the wake field effect remains finite for an ultrarelativistic beam due to resistivity of the accelerator walls and non-smoothness of the chamber (existence of RF cavities, bellows etc.). The effect of wake fields is an increasingly important issue since operating regimes are continually moving towards higher currents and

smaller bunches. If not properly dealt with, wake fields can lead to collective beam instabilities that limit a machine's performance. Therefore, an accurate numerical modeling of wake fields and their interaction with the beam is important for the development of high performance accelerator codes.

Two major sources of electromagnetic wake fields in an accelerator chamber are electric currents in resistive walls and non-smooth elements of the chamber (RF cavities, bellows etc.). We have developed a parallel software module for modeling the interaction of particle beams with wake fields. The corresponding theoretical model is based on analytical approximations in terms of the multipole moment expansion of the interaction of particle beams with wake fields induced on smooth resistive walls and non-smooth superconducting elements. The module has been implemented in MaryLie, an accelerator simulation code.

Notations and Definitions. The longitudinal and transverse wake field forces, integrated over a length L, acting on a test charge e, can be represented in terms of the longitudinal and transverse wake potentials, $W_m^{'}(z)$ and $W_m(z)$:

$$\begin{aligned} \int_{-L/2}^{L/2} ds\, \vec{F}_{\parallel} &= -eI_m W_m^{'}(z)\, r^m \hat{\mathbf{s}} \cos m\theta, \\ \int_{-L/2}^{L/2} ds\, \vec{F}_{\perp} &= -eI_m W_m(z)\, m r^{m-1} \left(\hat{\mathbf{r}} \cos m\theta - \hat{\boldsymbol{\theta}} \sin m\theta \right). \end{aligned} \tag{1}$$

where I_m are terms of the multipole moment decomposition of the beam charge density.

The Panofsky-Wenzel theorem implies

$$\nabla_{\perp} \int_{-L/2}^{L/2} ds\, \vec{F}_{\parallel} = \frac{\partial}{\partial z} \int_{-L/2}^{L/2} ds\, \vec{F}_{\perp}. \tag{2}$$

Impedances are Fourier transforms of wake functions:

$$\begin{aligned} Z_m^{\parallel}(\omega) &= \int_{-\infty}^{\infty} \frac{dz}{\beta c} \exp\left(\frac{-i\omega z}{\beta c} \right) W_m^{'}(z), \\ Z_m^{\perp}(\omega) &= \frac{i}{\beta} \int_{-\infty}^{\infty} \frac{dz}{\beta c} \exp\left(\frac{-i\omega z}{\beta c} \right) W_m(z). \end{aligned} \tag{3}$$

Due to the Panofsky Wenzel theorem,

$$Z_m^{\parallel} = \frac{\omega}{c} Z_m^{\perp}. \tag{4}$$

Numerical implementation. In the current numerical implementation, most of the accelerator chamber elements (resistive pipe, RF cavity etc.) have associated analytic wake field models valid under certain approximations. The resistive wall wake field model is valid if the skin depth is

much smaller than the thickness of the wall and requires only the wall conductivity. If the set of parameters required by a non-smooth element wake field model is unknown to the user (the quality factor and shunt impedance for an RF cavity, for instance), it is desirable to perform accurate numerical calculations of wake fields induced by this element, and to fit the corresponding analytical model to the numerical data. Such numerical calculations can be obtained using time domain electromagnetic codes (MAFIA, Tau3P etc.). Such analytic wake field models will be used to study multi turn beam dynamics in circular accelerators. To study the beam dynamics in linear accelerators, we will also use accurate precomputed and stored numerical data for wake fields induced on RF cavities and other non-smooth elements. This option was also implemented in the wake field module.

During the run time, the charge of a particle beam is being deposited on the 3d grid in the location of space charge nodes. This 3d charge distribution is used in the wake field module to calculate a user-defined number of miltipole moments I_m of the beam. These moments result from integration of the charge distribution (multiplied by some functions depending on m) in every transverse *x*-*y* plane of the grid along the *z*-axis. The computed and stored multipole moments are used to calculate the longitudinal and transverse forces due to wake fields in every grid point. The interpolation of the wake field forces from the grid to the location of every macroparticle is combined with the corresponding procedure for the space charge forces. The wake field algorithm takes into account long-range wake field forces that contribute during multiple turns of the beam.

Resistive wall wake fields. The resistive wake field forces decay slowly and contribute during multiple beam turns. The typical behavior of the longitudinal and transverse wake field functions and forces is given in Figures 3-4.

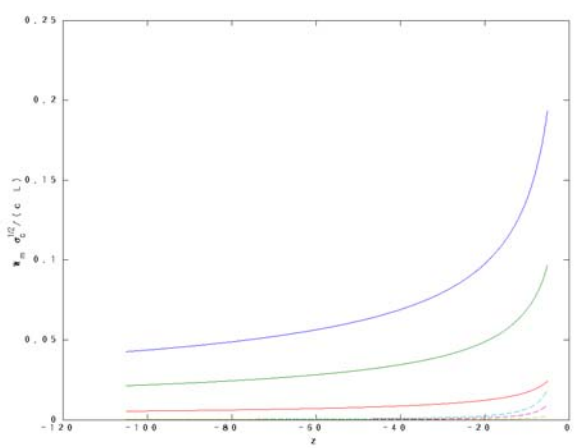

Figure 3. Longitudinal wake functions (solid lines) and transverse wake functions (dashed lines) for m = 0, 1, and 2.

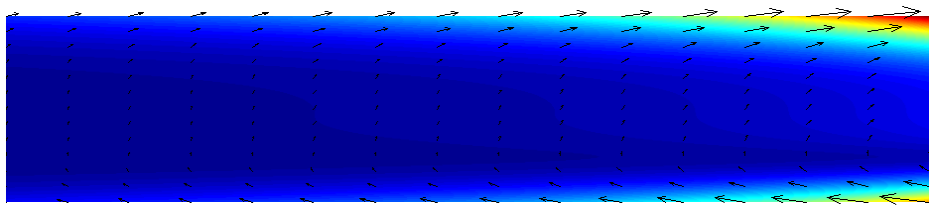

Figure 4. Distribution of wake field forces induced by an off-axial particle in a resistive pipe.

Wake fields in RF cavities. To study numerous beam dynamics problems, wake fields in RF cavities can be approximated with sufficient accuracy by the resonator model. The corresponding longitudinal wake function is

$$W_m^{'}(z)=\begin{cases} 0 & \text{if} \quad z>0, \\ \alpha R_s^m & \text{if} \quad z=0, \\ 2\alpha R_s^m e^{\alpha z/c}\left(\cos\dfrac{\varpi z}{c}+\dfrac{\alpha}{\varpi}\sin\dfrac{\varpi z}{c}\right) & \text{if} \quad z<0, \end{cases} \tag{5}$$

where $\alpha=\omega_R/2Q$ and $\varpi=\sqrt{\omega_R^2-\alpha^2}$. The transverse wake function for the region $z<0$ is

$$W_m(z)=\frac{cR_s^m\omega_R}{Q\varpi}e^{\alpha z/c}\sin\frac{\varpi z}{c}. \tag{6}$$

The behavior of the longitudinal impedance in the vicinity of resonator frequencies for different quality factors and the z-dependence of wake functions are shown in Figure 5**.**

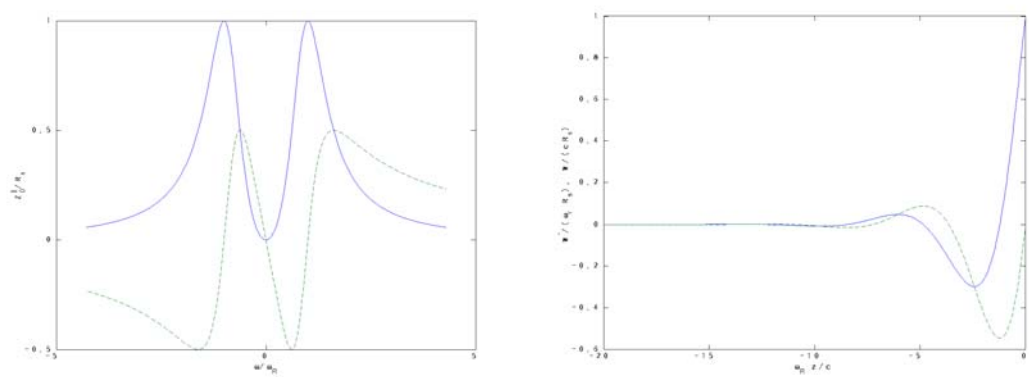

a) **b)**

Figure 5. a) Real part (solid line) and imaginary part (dashed line) of $Z_0^{\|}$ for a resonator model with Q=1. b) $W_0^{'}(z)$ (solid line) and $W_0(z)$ (dashed line) for resonator model with $Q=1$.

References

1. Chao, A.W. *Physics of Collective Beam Instabilities in High Energy Accelerators*. Willey, 1993.
2. Chao, A.W. and Tinger, M. *Handbook on Accelerator Physics and Engineering*. World Scientific, 1998.
3. Kurennoy, S. and Stupakov, G. Particle Accelerators **45**, 95 (1994).
4. Palumbo, L. and Vaccaro, V.G. Wake fields, impedances and Green's function. In S, Turner, Ed., *Advanced Accelerator Physics*. CERN 87-03, 1987.

Collaboration with BNL's Collider-Accelerator Department Computational Project

We have been working in collaboration with computational physicists at BNL's Collider Accelerator Department to develop Orbit, a PIC code for circular accelerators, which models collective beam effects through a "two-and-half" dimensional space charge problem [2,3]. The code is being applied for modeling of beam dynamics and instabilities in the AGS and SNS storage rings.

In the Orbit Code, a "herd" of randomly generated macro particles is pushed through a lattice represented by a sequence of maps. Once all particles have reached a certain location, their charge density is calculated by binning to a grid. The potential Φ is found by solving the Poisson equation with the perfectly conducting wall boundary conditions:

$$\Delta\Phi = -\frac{1}{\varepsilon}\rho, \quad \rho_{wall}(x, y, z) = 0. \tag{1}$$

Space charge force components (with coefficients to account for both the electrostatic and magnetic action) are calculated as derivatives of the potential and applied to each macro particle in the transverse direction. In a ring with long longitudinal bunches, the transverse motion can be uncoupled from the longitudinal one, and the Poisson problem can be solved in parallel in many longitudinal beam slices. Figure 6 shows a "frozen" beam at a given time in a simple FODO channel in the moment of the space charge calculation.

Several Poisson solvers have been implemented in the Orbit code. A direct integration of particle forces (brute force) gives a very transparent solution. However, this method has limitations: (1) arbitrary treatment of poles arising from the field points accidentally coincident with source points, (2) difficulties, including images on walls in the space charge calculation, and (3) length of execution. The Orbit code has the capability to solve the space charge problem by the FFT method. The method needs a grid twice the size of the beam to avoid aliases. Parallel differential solvers for the Poisson problem were implemented recently in the code based on the LU decomposition and an iterative (SOR) technique. The x- component of the space charge force calculated using different approaches is depicted in Figure 7.

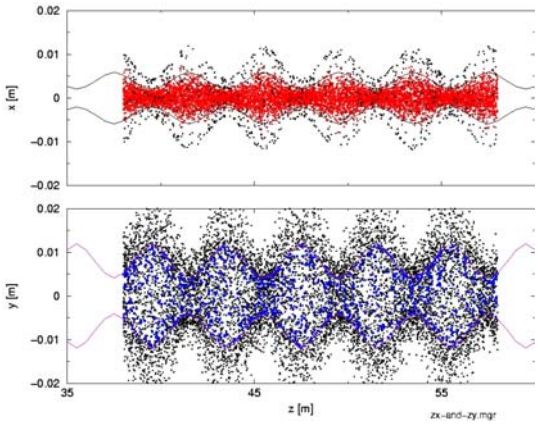

Figure 6. Frozen matched beam.
and the beam Envelope is also shown.

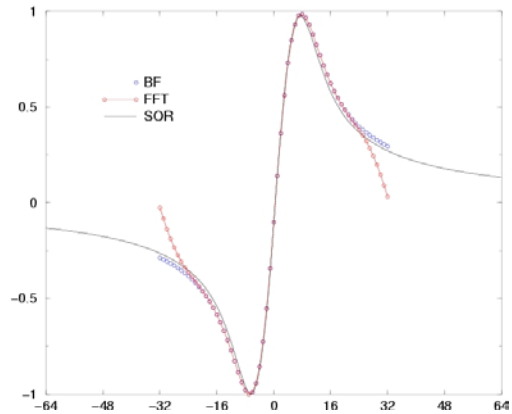

Figure 7. Space charge force component
calculated using different methods.

The parallelization of ORBIT, with the introduction of the space charge calculation in three dimensions, is structured around the concept of longitudinally partitioning the beam into equal length segments, the number of which can be varied. The parallelization had to possess the capability to handle almost any beam configuration ranging from coasting beams of uniform longitudinal density with lengths equaling the circumference of the machine to bunched beams of non-uniform longitudinal density with lengths a small fraction thereof. The development of an effective load balancing scheme is in progress. The 2D parallel performance of ORBIT was tested using the Brookhaven Galaxy Cluster. Linear performance scaling was observed with 32 processors.

References

1. Chao, A. *Physics of Collective Beam Instabilities in High Energy Accelerators*. John Wiley & Sons, Inc., New York, 1993.
2. Luccio, A. and D' Imperio, N. Tracking in accelerators with parallel computing. 6th International Accelerator Physics Conference, Darmstadt, Germany, Sept. 11-14, 2000.
3. Luccio, A., D'Imperio, N., and Samulyak, R. Solving by parallel computing the Poisson problem for high intensity beams in circular accelerators. *In Proc. Particles and Accelerators 2001*, June 18-22, 2001, Chicago, IL

4.2.3 High-Intensity Beam Simulation Project

This work has evolved from collaboration between the Beam Physics Group at GSI Darmstadt, Germany, and the SNS and AGS divisions and BNL. It emerges from the development of accelerators to higher intensities as drivers for spallation neutron sources, neutrino factories or radioactive beam facilities, which requires advancing beam simulation to larger scales.

Studies associated with high intensity beams have shown that phenomena associated with space charge, instabilities and beam loss have significant impact on the design of such projects. It is well established that accelerators involving a beam power of the order of 10 Megawatt or higher need

enormously improved control of beam loss beyond present experience. For protons of 1 GeV, for example, the tolerable loss of beam power corresponds to 1 W per m of the structure. This requires a reduction of the beam loss to as low as 10^{-6} in linacs and 10^{-4} in rings, which is far beyond the state-of-the-art of experiments as well as conventional approaches of computer modelling.

Beyond these application aspects the impact of high intensity on beam physics leads to challenging questions, where nonlinear dynamics of single particles gets linked with collective plasma (or space charge dominated) behavior including collisions and fluctuations. The analytical and computational modelling can learn from plasma physics and Hamiltonian mechanics to a certain extent, but new methods must be developed and applied. Characteristic features are the long time scales needed in accelerator beams, and the importance of resolving statistics up to one particle out of 10^6, which raises the issue of chaotic behavior in many-body systems.

Current specific projects are:

1. Studies of Mismatch Induced Halos: In high-intensity accelerators for protons or ions mismatch of beam envelopes leads to halo formation, which may be a source of beam loss due to aperture limitation. Most of the halo studies so far have considered round beams with axi-symmetric focusing. With anisotropy--caused by the ratios of focusing strengths and/or emittances different from unity--there is a strongly increased complexity in halo behavior due to an extension from a one-dimensional parameter space to a three-dimensional one (besides the 3D nature of the dynamical problem), which requires extensive simulation efforts.
2. Equipartitioning of Collisionless Beams: While beam plasmas normally can have different "temperatures" in the three degrees of freedom, we have found that under certain resonance conditions there is a collectively driven exchange of temperatures or emittances. This project is particularly relevant to high-intensity beams in linacs like the SNS linac.
3. Resonances in Circular Accelerators: Here the big challenge is the need to study up to 10^6 turns in synchrotrons for high intensity, which requires use of special simplifications as the "slicing" practiced in the ORBIT code developed at BNL.

References

1. Franchetti, G., Hofmann, I., and Jeon, D. Anisotropic free energy limit of halos in high intensity accelerators. Phys. Rev. Lett. **88**, 254802 (2002).
2. Hofmann, I., et al. Space charge resonances in 2D and 3D anisotropic beams. Submitted to Phys. Rev. ST Accel. Beams (2002).

4.2.4. MiniBooNE Detector Analysis

Introduction. The Booster Neutrino Experiment (BooNE) at Fermi National Accelerator Laboratory will investigate the neutrino mass by searching for neutrino oscillations from muon neutrinos to electron neutrinos. This will be done by directing a muon neutrino beam into the MiniBooNE detector and looking for electron neutrinos. This experiment is motivated by the oscillation results reported by the Liquid Scintillator Neutrino Detector (LSND) experiment at Los

Alamos National Laboratory. The major goal of the MiniBooNE experiment, the first phase of the BooNE project, is to confirm or refute the startling experimental results of the Los Alamos scientists. By changing the muon neutrino beam into an anti-neutrino beam, BooNE can explore oscillations from muon anti-neutrinos to electron anti-neutrinos. A comparison between neutrino and anti-neutrino results will tell us about CP- and CPT-violation.

The MiniBooNE detector is a sphere of 12 m diameter filled with mineral oil. Photomultiplier tubes (PMTs) are attached to the interior surface of the sphere with 55 cm spacing (see Figure 8). PMTs are vacuum glass containers with a 10 cm radius, sensitive to impacts of pressure waves in the container. The accident at another neutrino experimental facility in Japan, the Super-Kamiokande (SuperK) detector, raised many questions concerning the optimization of the design of such devices. About 60% of all photomultipliers used in the SuperK detector were destroyed in a few seconds due to shock waves in the container. Shock waves were induced by an accidental implosion of one PMT. The SuperK detector is a cylindrical tank filled with water and it uses 50 cm PMT's with 70 cm spacing. The accident forced a series of experiments to halt and required major repair work.

The aim of our numerical simulation project is to evaluate the stability of the MiniBooNE detector against PMT implosion induced shock waves. We will perform the numerical simulations of the PMT implosion process and the dynamics of shock waves in both MiniBooNE and SuperK geometries.

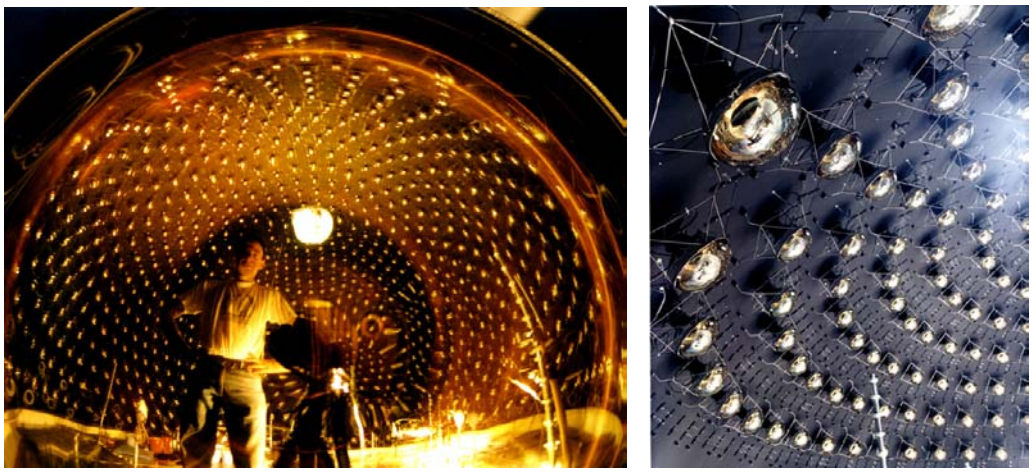

Figure 8. Inside the MiniBooNE detector (left) and arrays of photomultipliers (right).

Numerical simulations. We use the FronTier code for the numerical simulation of the PMT implosion and the dynamics of the reflected shock waves in the BooNE and SuperK containers. FronTier is a hydrodynamics code with free interface support. It is based on front tracking, a numerical method for the solution of systems of conservation laws which allows the computation of dynamically evolving interfaces through the solution of the corresponding Riemann problem. FronTier uses high-resolution hyperbolic methods for the interior domain away from free interfaces. It is capable of resolving contact discontinuities and fluid interfaces without mass diffusion. The code also uses realistic equation of state (EOS) models and stiff EOS models for fluids in particular.

We have performed preliminary studies of the PMT collapse and the shock wave dynamics in the MiniBooNE and SuperK containers. In the shock wave numerical experiment, the wave dynamics and pressure distribution in an array of 5 PMTs were studied. Shock waves were induced by implosion of the central PMT. The numerical simulation indicates stronger pressure waves on PMTs in the SuperK detector geometry compared to the MiniBooNE. However, adding the viscosity to the fluid (mineral oil was used in MiniBooNE) does not have a significant influence on the reduction of the shock wave strength. Numerical simulations suggest that the MiniBooNE detector is much more stable than the SuperK, and the chance for a chain collapse of PMTs in the MiniBooNE appears to be small.

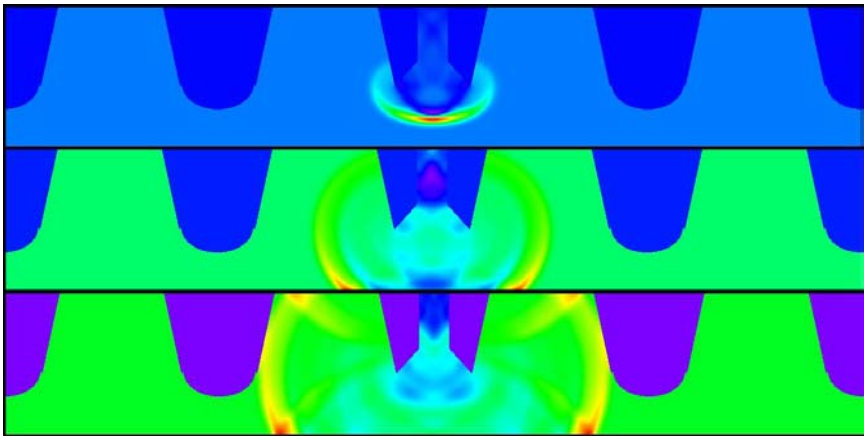

Figure 9. Dynamics of shock waves in the MiniBooNE container.

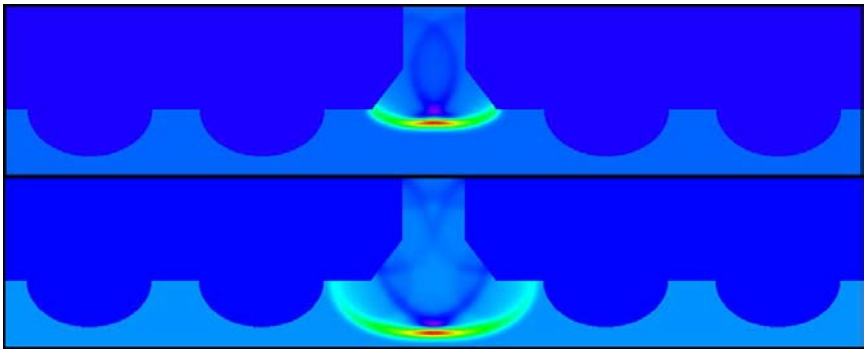

Figure 10. Dynamics of shock waves in the SuperK container.

4.3 BASIC ENERGY SCIENCES

The Department of Energy's Office of Basic Energy Sciences supports research in materials and chemical sciences, geoscience, engineering, and energy biosciences. This broad-based program of fundamental research is also responsible for a number of national user facilities, including synchrotron x-ray and neutron sources and electron microscope facilities. CDIC has engaged in numerous projects in computational fluid dynamics, many body physics, and optics, which are described here. See Table 5.

TABLE 5. CDIC BASIC ENERGY SCIENCES PROJECTS		
Project Title	**Key Personnel**	**Comments**
TSTT: Atomization and Spray	J. Glimm, M.N. Kim, A. Marchese, C. Tzanos, R. Samulyak, X. Li	Fuel Injection for Diesel Engine
Quantum Monte Carlo Simulations of Magnetic Systems	J. Davenport, I. Campos	Quantum Monte Carlo
Magnetic Nanowires	J. Davenport	Density Functional Theory
Superconductivity	J. Davenport	Density Functional Theory
Molecular Dynamics on the QCDOC	J. Davenport, Y. Deng, J. Glimm, E. Santos	Molecular Dynamics on the QCDOC
Uranium Equation of State	J. Davenport, N. Stojic	Density Functional Theory and Classical Monte Carlo
Numerical Simulation of Photonic Devices	J. Glimm, N. Stojic, N. D'Imperio	Parallel FDTD Maxwell Solver

4.3.1 TSTT: Atomization and Spray

Jet Breakup and Spray Formation in a Diesel Engine

The design of a fuel efficient, nonpolluting diesel engine is the subject of intensive international research efforts. The breakup of the injected jet of diesel fuel into spray is of key interest to such investigations because much of the pollution comes from unburned fuel deposited on the walls of the engine chamber, and because control of the spray droplet size can mitigate this effect. Spray formation is sensitive to many details of the injection system design, including the driving pressure in the nozzle, the nozzle shape, and the flow turbulence and phase transitions in the nozzle.

For the above reasons, a simulation study of the breakup of the diesel jet into spray is of considerable interest. Factors complicating such a study include:

1. the stiff equation of state (EOS) for the liquid diesel fuel;
2. presence of shock waves or near shock waves and phase transitions in the flow field;
3. the multiscale nature of the flow field, especially regarding turbulence in the nozzle and the multiscale breakup of the jet into droplets and spray; and
4. sharp boundaries for the liquid diesel fuel – ambient chamber gas interface for the duration of the breakup period.

We report preliminary progress on the numerical modeling of the jet breakup, based on the front tracking code FronTier. The work has been carried out by a team from BNL, ANL, and Stony Brook University. We modeled the diesel fuel as isentropic, with an analytic EOS. The EOS is given by a gamma law gas in the vapor region, by a stiffened gamma law gas in the liquid region, and by the homogeneous equilibrium model [5] along an isentrope in the mixed region (where vapor and liquid co-exist). *P vs. V* is graphed in Fig. 11.

Viscosity was added to the FronTier code, with an explicit algorithm and a parabolic CFL time step control, needed to control stability. For the presently considered meshes, the parabolic time step

control is nearly the same as the hyperbolic CFL constraint required for the Euler (hyperbolic) terms in the Navier Stokes equation. As the mesh is refined in future studies, the parabolic time step control will become limiting. Accordingly, we will first subcycle, and take smaller time steps in the parabolic terms alone, and with further mesh refinement, we will switch to a partly implicit algorithm.

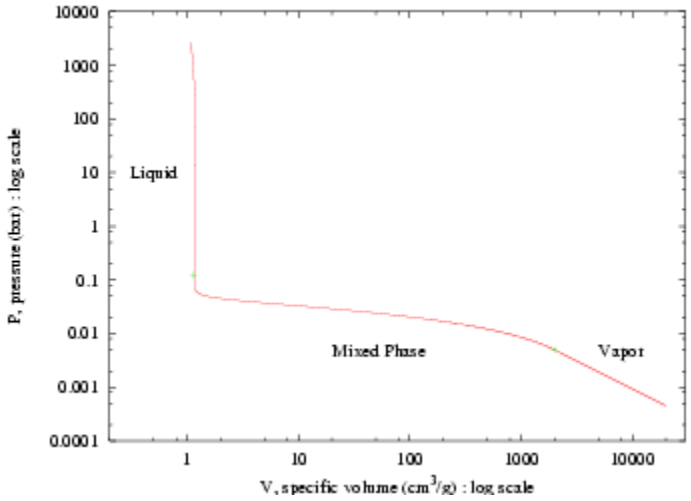

Figure 11. P *vs*. V isentrope for diesel fuel.

Slip and no-slip boundary conditions have been used in the fuel container and nozzle. More general possibilities will be considered in later stages of this work.

Figure 12 displays a detail in the experimental setup at ANL [1]. A finite pulse of diesel fuel is injected at a pressure of 500 bar into a chamber of SF6 (a heavy, inert gas chosen to simulate the compressed air in a diesel engine).

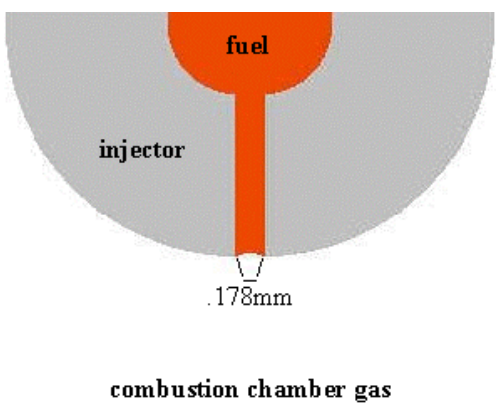

Figure 12. Geometry of injection reservoir and nozzle leading to combustion chamber.

Using synchrotron x-ray imaging, ANL scientists have measured the mass on line segments passing through the jet in both axial and radial directions. From this data they also note the velocities of the

tip and the tail of the fuel jet as it enters the combustion chamber [1, 2, 3, 4]. We have installed into our code diagnostics to record similar data in our simulations.

Figure 13 shows the density of the diesel fuel in preliminary simulation studies of the jet breakup [6]. As expected, the simulation shows the fuel cavitation at the nozzle inlet and continued phase transitions throughout the body of the jet.

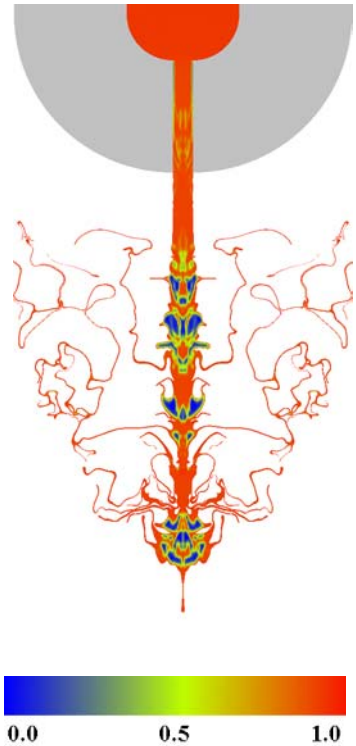

Figure 13. Density of diesel fuel as computed by *FronTier*.

Our present agreement with experiment is semi-quantitative. Some parameters not measured experimentally but important for simulation have been discovered. Parameter and mesh refinement studies are planned for future efforts. Our studies will include the following four aspects:

1. the initial pressure build-up of the fuel container (wave reflections and transmissions);
2. the response of the jet velocity to the applied pressure in the fuel container;
3. cavitation, one factor in formation of the spray;
4. entrainment, another factor for the formation of the spray.

References

1. MacPhee, A.G., Tate, M.W., and Powell, C.F. X-ray imaging of shock waves generated by high-pressure fuel sprays. Science **295**, 1261-1263 (2002).
2. Powel, C.F., Yue, Y., Gupta, S., McPherson, A., Poola, R., and Wang, J. Development of a quantitative measurement of a diesel spray core using synchrotron x-rays. In *Eighth International Conference on Liquid Atomization and Spray Systems, Pasadena, CA,* 2000.

3. Powel, C.F., Yue, Y., Poola, R., and Wang, J. Time resolved measurements of supersonic fuel sprays using synchrotron x-rays. J. Synchrotron Rad. **7**, 356-360 (2000).
4. Powel, C.F., Yue, Y., Poola, R., Wang, J., Lai, M., and Schaller, J. Quantitative x-ray measurements of a diesel spray core. In *Proc. 14th Annual Conference on Liquid Atomization and Spray Systems (ILASS), Dearborn, MI*, 2001.
5. Wallis, G. *One-Dimensional Two-Phase Flow*. McGraw-Hill, New York, 1969.
6. Glimm, J., Li, X.L., Oh, W., Kim, M.-N., Marchese, A., Samulyak, R., and Tzanos, C. Jet breakup and spray formation in a diesel engine. Proc. Second MIT Conference on Computational Fluid and Solid Mechanics, June 2003. Preprint number susb-ams-02-20. Submitted.

4.3.2 Quantum Monte Carlo Simulations of Magnetic Systems

The quantum mechanics of multi electron systems is fundamental to an understanding of magnetism. Progress on this problem will have profound implications for chemistry and condensed matter physics. Correlated electron systems are also important technologically. Materials containing manganese which display colossal magnetoresistance are likely candidates for high density storage devices; and superconductors with high transition temperatures could lead to enormous energy savings.

Considered naively, the correlated electron problem is exponentially hard because the number of states which must be considered grows exponentially with N, the number of electrons. Quantum Monte Carlo techniques have great promise because they reduce the multi electron problem to a sequence of single electron problems so that the overall effort scales roughly as the third power of N.

We have utilized the quantum Monte Carlo algorithm of Blancenbecler, Scalapino, and Sugar [1, 2] to study the single orbital Hubbard model in three dimensions with, typically, N = 64, 216, or 512 sites. The model is defined by the hopping parameter, t and the Coulomb interaction, U. For U = 0, the bandwidth or energy range of the allowed states is determined by t (it is 12t in 3 dimensions). For t = 0, the electrons are completely localized at sites.

This model displays a phase transition at low temperature to an antiferromagnetic ground state for U > 0. Because many actual antiferromagnets are layered structures, we have also varied the hopping between layers on the lattice. For zero interlayer hopping the model becomes two-dimensional, for which it is known that there is no phase transition (except at zero temperature).

Since the bulk of the computer time is spent on matrix multiplication we have paid special attention to this aspect. Loop unrolling keeps data within the cache on our Linux cluster. Systematic cache optimization is provided by the Automatically Tuned Linear Algebra Software (ATLAS) library [3]. We have developed two ways to parallelize the code. For small or large systems, multiple copies of the code can be run on different processors with different random number seeds, generating independent sequences of states. For larger systems, the matrix and its multiplication is distributed over a set of processors so that the same random numbers apply to each. Each processor can then perform the required matrix operations on a subset of the matrix elements. Clearly the two parallelization methods can be combined if desired.

The algorithm requires the inversion of matrices which become nearly singular for low temperatures. Following White et al. [2] we have implemented a scheme which uses singular value decomposition of the matrices and greatly expands the accessible temperature range.
To search for the phase transition we have studied the staggered magnetization as a function of temperature. The magnetization, or average value of the spin, is nearly zero since for antiferromagnets the spins point alternately up and down on adjacent lattice sites. The staggered magnetization is formed by taking the average spin but inverting it on every other site. It would be one for a classical antiferromagnet (and zero for a ferromagnet where all the spins are parallel or for an antiferromagnet at high temperatures where the order has been lost). The staggered magnetization is shown versus temperature (in units of t, the hopping parameter) in Figure 14 for a 4x4x4 = 64 site cluster with periodic boundary conditions.

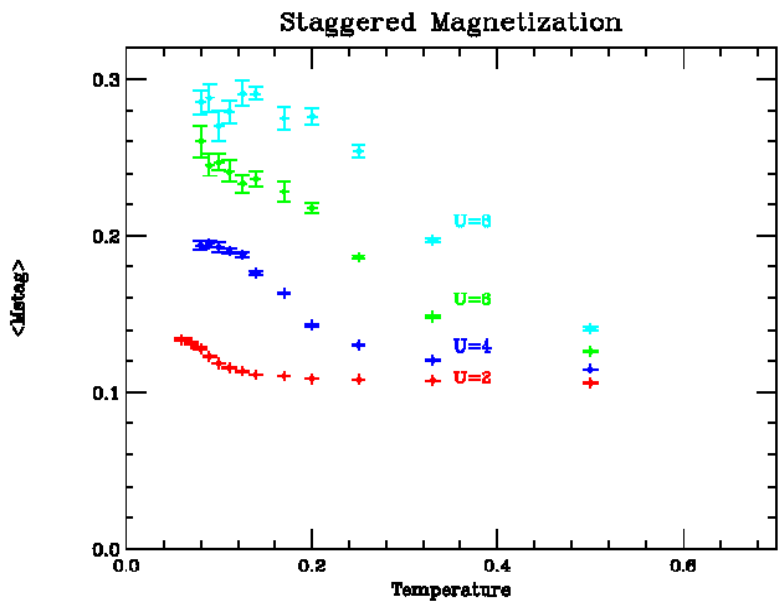

Figure 14. Staggered magnetization versus temperature, T for a 4x4x4 lattice. T and U are in units of t, the hopping parameter.

As the Coulomb interaction U increases, the magnetization becomes larger because the electrons are more localized. The rise in magnetization as the temperature decreases is the result of ordering. The phase transition temperature is near the midpoint of the rise. However, the best way to determine the temperature is to study magnetic susceptibility versus temperature. Results of such a study are shown in Figure 15 and compared with previous work. As can be seen, the new results give a significantly lower transition temperature than that found previously. We attribute this fact to the availability of longer runs, the use of periodic boundary conditions, and the utilization of the susceptibility to determine the phase transition. Further work on larger lattices is needed to confirm this result.

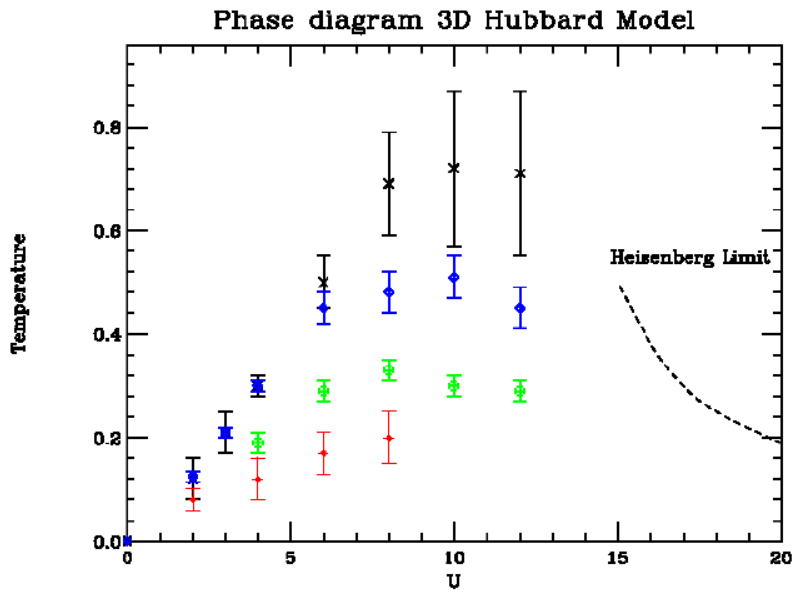

Figure 15. Neel temperature versus U (both in units of t): red - current work [8], black [4], blue [5], and green [6] are previous quantum Monte Carlo results. The curve at layer L is the result for the Heisenberg model [7].

The single orbital Hubbard model has contributed greatly to our understanding of magnetic and superconducting systems but essentially all real magnets involve more than a single orbital. In order to compare with actual experiments, our future plans call for the study of the multi orbital Hubbard model with realistic values of the parameters.

We also plan to extend the message passing parallelization scheme to one involving a mixture of message passing and threads to take advantage of heterogeneous memory access common in high-performance computing.

References

1. Blankenbecler, R., Scalapino, J.D., and Sugar, R.L. Monte Carlo calculations of coupled boson-fermion systems. I. Phys. Rev. D **24**, 2278 (1981).
2. White, S.R., Scalapino, D.J., Sugar, R.L., Loh, E.Y., Gubernatis, J.E., and Scalettar, R.T. Numerical study of the two-dimensional Hubbard model. Phys. Rev. B **40**, 506 (1989).
3. www.netlib.org/atlas/
4 Hirsch, J.E. Simulations of the three-dimensional Hubbard model: Half-filled band sector. Phys. Rev. B **35**, 1851 (1987).
5. Scalettar, R.T., Scalapino, D.J., Sugar, R.L., and Toussaint, D. Phase diagram of the half-filled 3D Hubbard model. Phys. Rev. B **39**, 4711 (1989).

6. Staudt, R., Dzierzawa, M., and Muramatsu, A. Phase diagram of the three-dimensional Hubbard model at half filling. Eur. Phys. J. B **17**, 411 (2000).
7. Sandvik, A.W. Critical temperature and the transition from quantum to classical order parameter fluctuations in the three-dimensional Heisenberg antiferromagnet. Phys. Rev. Lett. **80**, 5196 (1998).
8. Campos, I. and Davenport, J. Monte Carlo study of the magnetic properties of the 3D Hubbard model. Cond-mat/0112254.

4.3.3 Magnetic Nanowires

Magnetism in One-dimensional Nanowires

Nanotechnology allows structures of a limited number of atoms that may play an important role in future applications, such as spintronics, magneto-optical devices, and quantum computers. The experimental efforts require extensive theoretical support because the results of recent measurements open many questions which remain to be answered. Magnetism in low-dimensional systems such as monatomic nanowires, namely linear chains of magnetic atoms, grown on non-magnetic substrates is particularly interesting. Cobalt chains adsorbed on platinum surfaces display magnetic order which has been studied by *ab-initio* calculations and experimentally by x-ray magnetic circular dichroism (XMCD) using synchrotron radiation. These systems display the largest orbital magnetic moment ever found in a 3d transition element.

A numerical simulation within the framework of the density functional theory is of great importance in order to interpret these experiments correctly. We apply the super-cell technique, where the nanowires are modeled as a repeat structure, shown in Figure 16. Such a structure with a stepped-substrate surface mimics the real material fairly well. The chosen inter-chain distance is large enough to avoid interactions between different wires. The calculations are performed using the full-potential linearized-augmented-plane-wave (FLAPW) method [2]. The wave functions are calculated in the scalar-relativistic approximation, while the spin-orbit coupling, essential for the XMCD effects, is included as a perturbation with the second-variational method. In the same manner, we optionally include an orbital-polarization (OP) term [3, 4], which takes partial account of the correlation effects associated with Hund's rule. The local-spin-density approximation (LSDA) is used for the exchange-correlation potential. Figure 17 shows the spin density, calculated as the difference in the charge density for the electrons with up and down spins. Besides the large peaks at the sites of the Co atoms, there are also lower peaks in the spin density at the sites of the Pt atoms. The magnetization is obviously induced in the substrate, which partly explains the existence of ferromagnetism in the quasi one-dimensional wires.

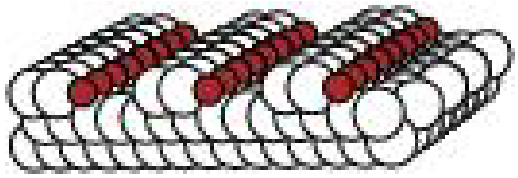

Figure 16. Periodic structure of the cobalt chains (red spheres) on the platinum surface.

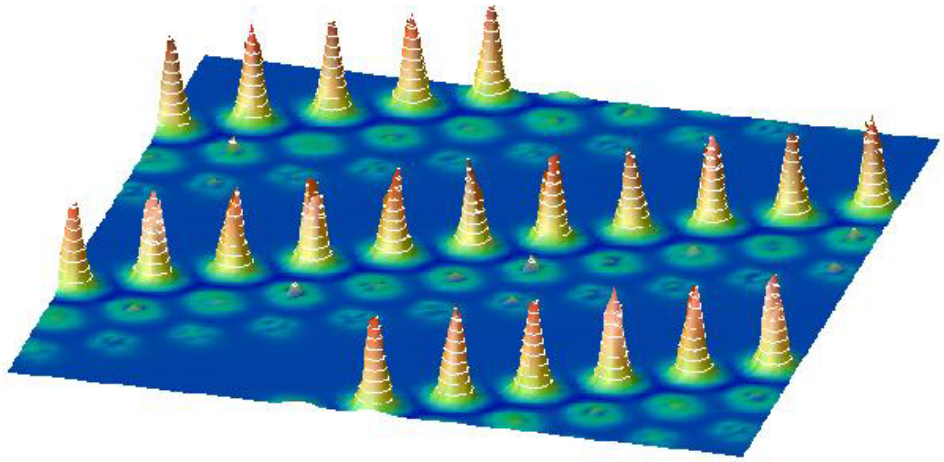

Figure 17. Calculated spin density of the cobalt nanowires on platinum.

References

1. Gambardella, P., Dallmeyer, A., Maiti, K, Malagoli, M. C., Eberhardt, W., Kern, K., and Carbone, C. Ferromagnetism in one-dimensional monoatomic metal chains. Nature **416**, 301 (2002).
2. Blaha, P., Schwarz, K., Madsen, G., Kvasnicka, D., and Luitz, J. WIEN2k, an augmented plane wave + local orbitals program for calculating crystal properties (Karlheinz Schwarz, Techn. Universitat Wien, Austria), 2001. ISBN 3-9501031-1-2.
3. Komelj, M., Ederer, C., Davenport, J. W., and Fahnle, M. From the bulk to monatomic wires: An ab-initio study of magnetism in Co systems with various dimensionality. Phys Rev B, in press.
4. Ederer, C., Komelj, M., Davenport, J.W., and Fahnle, M. Comment on the analysis of angular-dependent x-ray magnetic circular dichroism in systems with reduced dimensionality. Submitted.

4.3.4 Superconductivity

Charge Distribution in the Superconductor Magnesium Diboride

MgB_2 has recently been found to display superconductivity at the surprisingly high temperature of 39K [1]. This has stimulated a large research effort to determine the cause of the high transition temperature, as well as other properties of this otherwise unremarkable material. We have utilized first principles density functional theory to calculate the charge density in MgB_2 and compare it with transmission electron microscope and synchrotron x-ray measurements carried out at Brookhaven.

MgB_2 forms in a hexagonal crystal structure, with the boron atoms arranged in a honeycomb fashion in planes that are structurally the same as graphite. The magnesium atoms are located in the hollow positions in parallel planes above and below.

We have used the full potential linear augmented plane wave (FLAPW) method to solve the density functional equations [2]. The calculated lattice constants are in good agreement with previous calculations and with experiments. The same technique had been used earlier to study the distribution in energy of the occupied and empty states [3].

Figure 18 shows a contour plot of the difference charge density in the boron plane [4]. The difference density is obtained by subtracting the density of isolated atoms from that of the compound. The red areas between the atoms show clearly the build up of the bond charge.

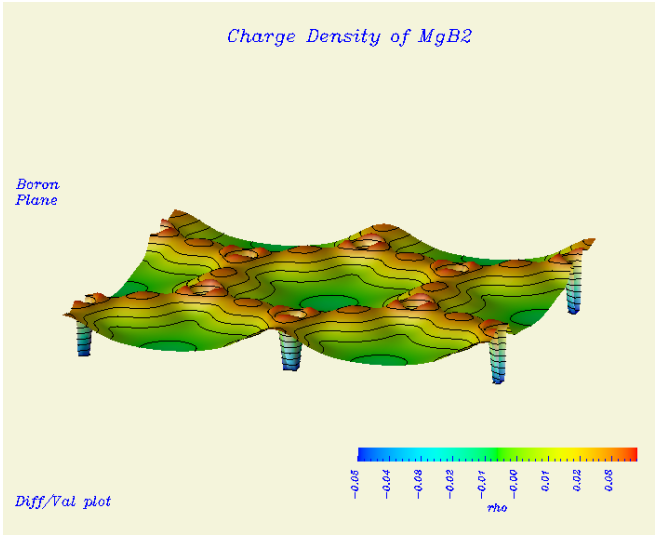

Figure 18. Charge density contours in the hexagonal compound MgB_2 calculated from first principles density functional theory.

Experiments measure the structure factors of the charge distribution, which are related to the Fourier transform of the density. The calculations described here agree with the experiments to within 3%. Further, calculations using only the atomic density, which are typically used in diffraction experiments, disagree with the data by up to 28%, clearly showing the importance of quantum mechanical calculations of x-ray diffraction. We have also studied the details of the x-ray absorptive edge finding excellent agreement with experiments [5].

References

1. Nagamatsu, J., Nakagawa, N., Muranaka, T., Zenitani, Y., and Akimatsu, J. Superconductivity at 39K in magnesium diboride. Nature **410**, 63 (2001).
2. Blaha, P., Schwarz, K., Madsen, G., Kvasnicka, D., and Luitz, J. WIEN2k, an augmented plane wave + local orbitals program for calculating crystal properties (Karlheinz Schwarz, Techn. Universitat Wien, Austria), 2001. ISBN 3-9501031-1-2.
3. Zhu, Y., Moodenbaugh, A. R., Schneider, G., Davenport, J. W., Vogt, T., Li, Q., Gu, G., Fischer, D. A., and Tafto, J. Unraveling the symmetry of hole states near the Fermi level in the MgB2 superconductor. Phys. Rev. Lett. **88**, 247002 (2002).

4. Wu, L., Zhu, Y., Vogt, T. Su, H., Davenport, J. W., and Tafto, J. Valence electron distribution in MgB2 studied by accurate diffraction measurements and first principle calculations. Submitted.
5. Moodenbaugh, A.R., Fischer, D.A., Li, Q., Gu, G., Zhu, Y., Su, H., Welch, D.O., and Davenport, J.W. X-ray absorption study of the boron K near edge in MgB2. Submitted.

4.3.5 Molecular Dynamics on the QCDOC

Molecular dynamics simulations [1, 2] are ideal for massively parallel computing because the time spent on communication can be a small fraction of the time spent on computation. However, most molecular dynamics (MD) simulations have been performed on machines where this potential has not been realized because of slow communication and/or small number of processors.

We have explored [4] the use of a new machine designed for quantum chromodynamics (QCD) by a team of elementary particle physicists [3] mainly at Columbia University, The Riken BNL Research Center and IBM. This machine consists of approximately 10,000 IBM PowerPC processors with extremely fast nearest neighbor communication and 4 megabytes of memory located on the same chip. For this reason it has been named QCDOC for quantum chromodynamics on a chip. It is expected to achieve of order 5 teraflops (or 5×10^{15} floating point operations per second) at a cost of roughly $500 per processor.

There are two broad classes of MD simulations in use. In materials science it is common to use embedded atom potentials which are density dependent but of relatively short range. For these, the nearest neighbor architecture can be exploited directly and we find that calculations on 10^6 atoms with simulation times up to 10 microseconds are feasible with 5 - 6 weeks of computing time. The second class, typical of biomolecules, involves long-range forces (such as 1/r, or dipolar), but the system sizes are typically smaller, of order 50,000 atoms. For these we plan to utilize the Ewald method, which splits the interaction into a short- and a long-range part. The short-range part is treated as before and the long-range part is treated as a Fourier sum. The latter requires communication among all the processors, but because of the high dimensionality of the links (i.e., 6) and the store and forward feature of the machine, simulations of up to a microsecond are feasible [4].

These simulations are important in areas such as nanoscience chemistry and biology where the complexity of the atomic arrangements, the difficulty in performing experiments in non crystalline environments, and the need to understand crystal growth and other dynamic processes are crucial.

References

1. Allen, M. P. and Tildesley, D.J. *Computer Simulation of Liquid.* Oxford, New York, 1987.
2. Frenkel. D. and Smit, B. *Understanding Molecular Simulation*. Academic, San Diego, 1996.
3. Chen, D., Christ, N.H., Cristian, C., Dong, Z., Gara, A., Garg, K., Joo, B., Kim, C., Levkova, L., Liao, X., Mawhinney, R.D., Ohta, S., and Wettig, T., hep-lat/0011004.
4. Davenport, J.W., Deng, Y., Glimm, J., and Santos, E. On the use of the quantum chromodynamics computer for classical molecular dynamics with Coulomb potentials. Technical Report.

4.3.6 Uranium Equation of State

Introduction

Uranium, being the only commercially produced radioactive mineral, has been interesting to the scientific as well as to the general community. It is used for the generation of electricity and the production of radioisotopes for medical uses. Considerable attention has been given to the study of uranium compounds (uranite, pitchblende, brannerite, coffinite) in contrast to the studies of its pure metallic state. Metallic uranium has an interesting complex crystal structure, as is shown in Figure 19. It is the only nonmagnetic element known to form an incommensurate charge density wave state at low temperatures. At room temperature it crystallizes in an orthorhombic structure, and on heating passes through tetragonal and body centered cubic phases before melting at 1408K. As one of the actinides, it has partially filled 5*f* states, yet unlike the 4*f* (rare earth) elements and the heavier actinides, the 5*f* electrons are believed to be relatively delocalized and contribute to the metallic bond. Many uranium alloys display heavy fermion behavior, indicating some form of incipient localization.

In this work we have used first principles density functional theory, including the spin orbit interaction, to calculate the structural energies and bulk moduli of the competing phases. We have then fitted these to an embedded atom potential and plan to perform molecular dynamics simulations to obtain temperature dependent properties, such as the melting temperature and the coefficient of thermal expansion.

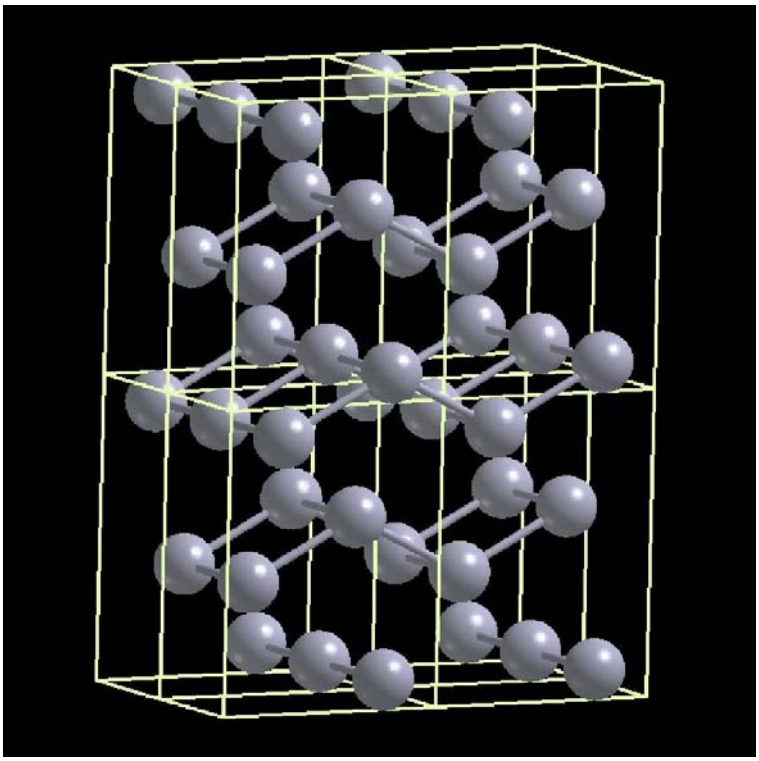

Figure 19. α-uranium.

Surprisingly, we have found that the BCC phase is mechanically unstable, which is to say that the energy surface has negative curvature for tetragonal distortions, as can be seen in Figure 20. It is energetically favorable to change the crystal structure into body centered tetragonal, by varying the ratio of crystal lattice constants. Describing the mechanical stability of nonequilibrium phases is important for phase diagram construction, structure of grain boundaries and epitaxial thin films.

Ab initio Calculations

To obtain the structural energies we used the full potential linearized augmented plane wave method as embodied in the WIEN2k code [1]. This is widely recognized as the most accurate method for solving the density functional equations (a set of single particle equations obtained by reduction from many body problems applying the density functional theory). The WIEN2k code includes local orbitals to better describe semi core states. We also used the generalized gradient approximation (GGA) for exchange and correlation as described by Perdew et al. in [3]. The GGA has been related to a significant improvement in the calculated volume compared with experiment [4]. Structures studied included the simple, face centered, and body centered cubic, body centered tetragonal, orthorhombic, and hexagonal close packed. We determined the cohesive energy, equilibrium volume, and bulk modulus for each structure. Structural energy differences and vacancy formation energy for the BCC lattice were also found.

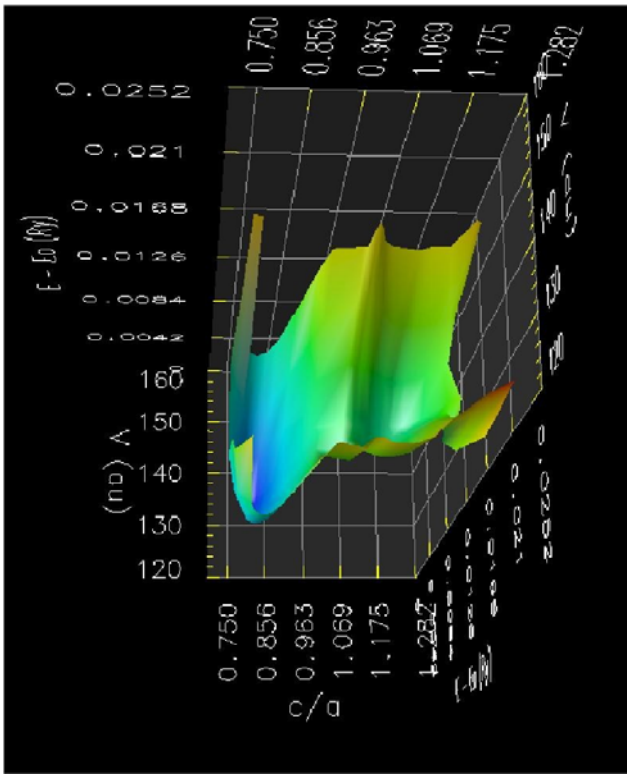

Figure 20. Mechanical stability of the BCC structure. The energy is shown as a function of unit cell volume and ratio of lattice axes c/a. We changed the c/a ratio, thus deforming the BCC structure ($c/a = 1$) into a body-centered tetragonal lattice structure, which is at a minimum, at $c/a = 0.8123$ and $V = 139.3703$ bohr^3.

Embedded Atom Method

In this model, proposed by Daw and Baskes [6], the total energy is divided into a pairwise interaction ϕ and an embedding energy F which is a function of the density ϕ:

$$E_{tot} = \sum_i F_i(\rho) + \frac{1}{2}\sum_{i,j}\phi(r_{i,j}) \tag{1}$$

For two-body central potential between the atoms i and j, with the separation distance r_{ij} we have used the Morse potential form:

$$\phi(r_{ij}) = E_1\left[\exp\left[-2\alpha\left(\frac{r_{ij}}{r_0}-1\right)\right]-2\exp\left[-\alpha\left(\frac{r_{ij}}{r_0}\right)-1\right]\right] \tag{2}$$

where E_1, α, and r_0 are adjustable constants.

The embedding function is represented by a polynomial:

$$F(\rho) = F^{(0)} + \frac{1}{2}F^{(2)}\left(\rho-1\right)^2 + \sum_{n=1}^{4}F^{(n+2)}\left(\rho-1\right)^{n+2} \tag{3}$$

for $\rho < 1$ and

$$F(\rho) = \frac{F^{(0)} + \frac{1}{2}F^{(2)}\left(\rho-1\right)^2 + F^{(3)}\left(\rho-1\right)^3 + Q^{(1)}\left(\rho-1\right)^4}{1+Q_2\left(\rho-1\right)^3} \tag{4}$$

for $\rho > 1$. $F^{(0)}$, $F^{(2)}$ - $F^{(6)}$, $Q^{(1)}$, $Q^{(2)}$ are fitting parameters, as is proposed by Mishin et al. [7]. Electron density is replaced by an exponentially decaying function. We include interactions up to a second neighbor in the BCC lattice, and for further distances we use an attenuating cutoff function.

The fitting parameters were chosen in such a way that the EAM results match the results obtained by the first principles calculations. Two structural energy differences were used to test the validity of the fits.

References

1. Blaha, P., Schwarz, K., and Luitz, J. *WIEN97, A Full Potential Linearized Augmented PLane Wave Package for Calculating Crystal Properties.* (Karlheinz Schwarz, Technical Universit@t Wien, Austria, 1999). ISBN 3-9501031-0-4.
2. Kokalj, A. J. Mol. Graphics Modelling **17,** 176 (1999).
3. Perdew, J.P., Burke, S., and Ernzerhof, M. Phys. Rev. Let. **77**, 3865 (1996).
4. Jones, M.D., Boettger, J.C., and Albers, R.C. Phys. Rev. B **61**, 4644 (2000).
5. S`derlind, P. Phys. Rev. B **66**, 085113 (2002).

6. Daw, M.S. and Baskes, M.I. Phys. Rev. Lett. **50**, 1285, (1984).
7. Mishin, Y., Mehl, M.J., Papaconstantopoulos, D.A.,Voter, A.F., and Kress, J.D. Phys. Rev. B **63**, 224106 (2001).

4.3.7 Numerical Simulation of Photonic Devices

Photonic crystals are a novel class of optical materials fabricated with at least two different dielectric permittivities in a periodic arrangement. They have the ability to suppress, enhance, or otherwise control the emission of light in a selected frequency range by altering the density of states. A complete photonic band gap (PBG), i.e. a range of frequencies for which light cannot propagate through the crystal in any direction, is a spectral region where the density of states in an infinite crystal vanishes. Photonic structures have a number of potential applications: light emitting diodes, low loss optical devices with increased extracting capability (high Q, low volume and thin cavities, surface grating couplers), lasers, waveguides, low-loss waveguide bends, junctions, couplers and many more.

We have developed a simulation algorithm for photonics, capable of handling complex geometry, realistic initial and boundary conditions, finite size effects, dispersive and nonlinear media, and surface waves. Our primary focus is on the simulation of realistic experimental structures, such as waveguides, photonic band gaps, and totally reflecting boundaries. We used the finite-difference time-domain method to solve the Maxwell equations.

We use a mesh that is divergence-free with respect to its electric and magnetic fields, and suitable for specifying field boundary conditions and singularity [1]. We developed a parallel code which was run on the Brookhaven Galaxy cluster. The calculational domain consists of 19 photonic lattice cells in the periodic structure for the dielectric constant in the x and y directions and 1/5 of a photonic cell in the z direction. Periodic boundary conditions were used in all three directions. Each photonic lattice cell has been divided into 40x40 computational mesh cells, but due to duality of the calculational mesh (see Yee, [1]), we effectively calculated each field on only 20x20 points inside a photonic lattice cell. The period of the oscillation was divided into 90 time steps of the numerical integration. A typical 50-period (4500 time steps) run took 50 minutes.

We have applied this algorithm to study the localized transverse magnetic (TM) defect modes in a two-dimensional, triangular-lattice photonic crystal [2]. The sample consists of an array of circular air-cylinders in a dielectric medium (chosen to represent gallium arsenide). To validate our computations, the results for the transverse electric (TE) case were checked against experimental and numerical results using a different method. We study the spatial symmetry for the TM modes, obtained by changing the dipole excitation frequency. Also, we varied the defect-cylinder radius to tune the resonant frequency across the band gap. The TM mode is found to be highly localized at the defect in the photonic lattice. Figure 21 shows the spatial distribution of the magnetic field for the E1 and B2 modes. Figure 22 illustrates the eigen frequency dependence on the radius of the defect rod.

Currently, we are applying our results on defect modes and localization effects to laser structures. The novel aspects of this study are the choice of a different geometry, new absorbing boundary conditions, and resulting different modes.

(a) (b)

Figure 21. The spatial distribution of the magnetic field after 100 oscillation periods for two modes: (left) E1 mode [scaled angular frequency a/8 = 0.411 (a is the lattice constant and 8 is the wavelength of the oscillating electric field)] and (right) B2 mode (a/8 = 0.48).

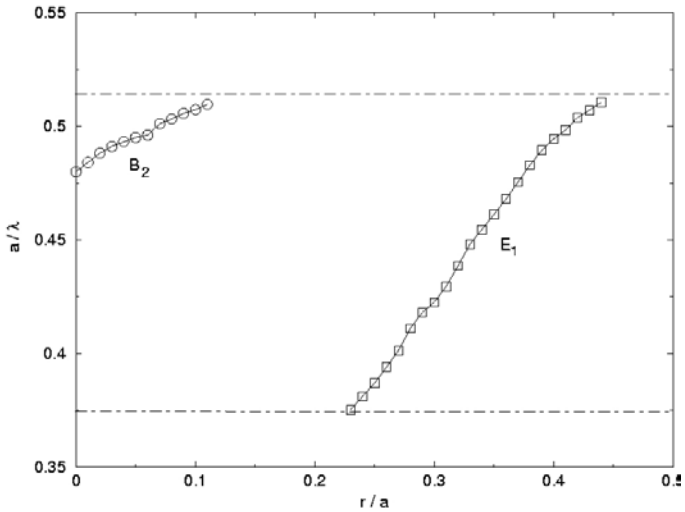

Figure 22. The eigen frequency of the localized defect modes as a function of the defect rod. The ordinate is the normalized frequency and horizontal lines represent the boundaries of the photonic band gap.

References

1. Yee, K.S. Numerical Solution of Initial Boundary Value Problems in Isotropic Media. IEEE Trans. Antennas and Propagation **14**, 302 (1996).

2. Stojic, N., Glimm, J., Deng, Y., and Haus, J.W.. Transverse magnetic defect modes in two-dimensional triangular-lattice photonic crystals. Physical Review E **64**, 1-7, Paper #056614 (2001).

4.4 BIOLOGICAL AND ENVIRONMENTAL RESEARCH

See Table 6 for a list of projects.

Brookhaven has strong experimental programs in atmospheric chemistry and in brain physiology. Both programs are data intensive. The data challenge is not only data quantity, but especially data understanding. We are developing new tools for the visual and statistical analysis of data and we are actively using these tools in the search for scientific understanding. The tools themselves are based on advanced and novel concepts in computer science and statistics. See also Section 4.5.3.

TABLE 6. BIOLOGICAL AND ENVIRONMENTAL RESEARCH PROJECTS

Project Title	Key Personnel	Comments
Parallel Atmospheric Aerosol Model	C. Benkovitz, J. Luo, H. Qin, S. Schwartz, L. Slatest	Aerosols in Climate
Neuron Imaging	B. Lindquist, M. Vazquez, C. Weaver	Edge Detection Image Analysis
Cardiac Electrophysiology	S. Evans, F. Fenton, J. Glimm, H. Hastings, W. Oh	Fibrillation, Sudden Cardiac Death

4.4.1 Parallel Implementation of an Atmospheric Aerosol Model

We have been working to construct a parallel version of an atmospheric aerosol model to describe global sulfate and SO_2 concentrations [1]. The model tracks the distribution of pollution and naturally produced aerosol particles to various parts of Earth's atmosphere. Archived weather data along with emissions data serve as input to the model.

There is emerging evidence that these aerosol particles exert a cooling influence on the Earth's climate. The direct aerosol effect involves the scattering of solar radiation off these particles and back into space. The indirect effect occurs when clouds form where a greater concentration of aerosol particles are present. Such clouds tend to have a greater concentration of cloud droplets, which also scatter solar radiation.

The model is a 3D Eulerian transport code which also includes chemical reactions among 25 different species. Pollutants are transported by (externally supplied) velocity fields and allowed to react within each cell according to the local temperature (also externally supplied). The hemispherical model has one-degree resolution, so the grid has 360 points for longitude and 81 for latitude, with 27 vertical levels.

The relatively large size of the grid leads to a large array of data points, e.g., 360x81x27x25 = 19,683,000 numbers or approximately 150 megabytes in double precision. This is for a single time

step. This problem is an ideal candidate for parallelization since much of the processor time is spent on the chemistry within a single cell, and relatively little time is spent on communication among cells. In addition, the communication that does occur is between a cell and its nearest neighbors. Consequently, a parallel version of the model is now under development for use at the National Energy Research Scientific Computing Center at Lawrence Berkeley National Laboratory, on their IBM SP. This parallel version distributes the longitudinal grid points across processors. The parallel version uses MPI (Message Passing Interface) to communicate data among the cells (e.g., the nodes of the NERSC IBM SP). It uses MPI/IO, defined in the MPI-2 standard, to perform input/output operations. Among its advantages, MPI I/O affords a convenient way to read an input file using a different number of processors than were used to write it.

Reference

1. Benkovitz, C.M. and Schwartz, S.E. Evaluation of modeled sulfate and SO_2 over North America and Europe for four seasonal months in 1986-87. J. Geophys. Res. **102,** 25305-25338 (1997).

4.4.2 Neuron Imaging

We have developed a numerical method to analyze digitized microscope images of retinal explants and quantify neurite outgrowth [1]. Few parameters are required as input and limited user interaction are necessary to process an entire experiment of images. This eliminates fatigue-related errors, user-related bias, and labor-related data analysis limitations common to manual analysis, while providing results that are nearly identical. The method does not require stained images and it handles images of variable quality. The crux of our algorithm lies in tracing the ridges of a polar function of greyscale intensity, which represent the neurite outgrowth. See Figure 23 to compare automatic and manual analysis of a retinal explant culture.

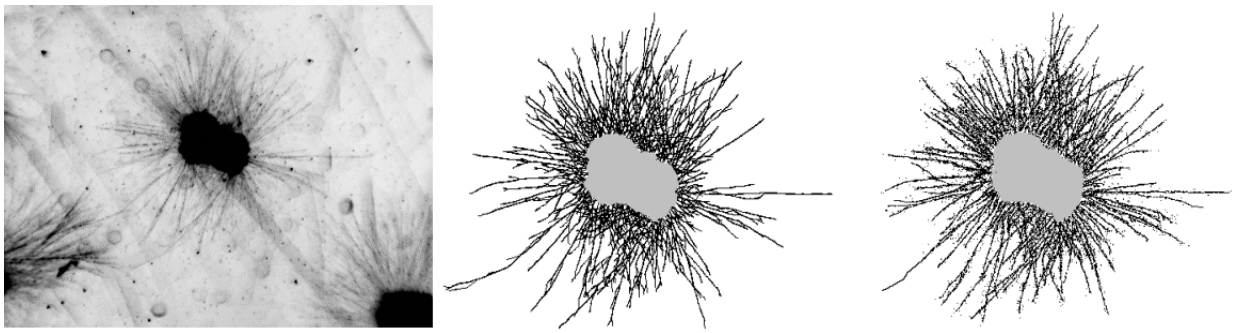

(a) (b) (c)

Figure 23. (a) A digitized microscope image, (b) automatic reconstruction of the explant region and neurite outgrowth, as compared with (c) manual analysis.

The method has been used to assess the neurotoxicity in retinal explants of high-energy iron particles found in galactic rays. This assessment will help to determine whether the heavy ion

component of these rays might inactivate critical cells in the brain that could not be repaired or replaced by the body. As shown in Figure 24, no significant neurotoxic effect is detected prior to 72 hours after explantation; at 72 hours significant growth reduction compared to the control is observed at even the smallest radiation dose.

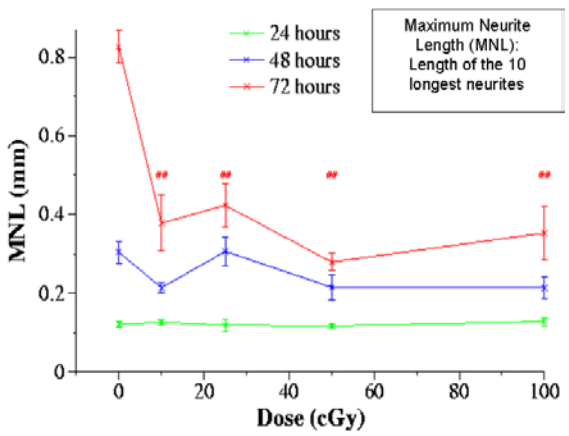

Figure 24. Automated analysis of the time-dependent effects of the dosage of 1 GeV/nucleon Fe ions on maximum neurite length. No significant effect is detected prior to 72 hours after explantation; at 72 hours significant growth reduction compared to the control is observed at all radiation doses.

Future work includes determining the effects of shielding on the neurotoxicity, as well as determining neurotoxicity of various ions as a function of linear energy transfer (LET). Shielding the explant cultures from the ion beam may reduce the neurotoxic response, may show no significant reduction, or may even further inhibit neurite growth. In the LET study, it is expected that a high-LET ion will have a greater neurotoxic effect on the explant cultures than a lower-LET ion at the same radiation dose. Additionally, the algorithm is being modified to quantify neurite outgrowth from individual neuron cells (see Figure 25 for preliminary results), in order to study the cellular morphological responses induced by methamphetamine (METH). We expect that increasing doses of METH will result in reduced neurite outgrowth. This research was supported in part by a grant from the Swartz Foundation.

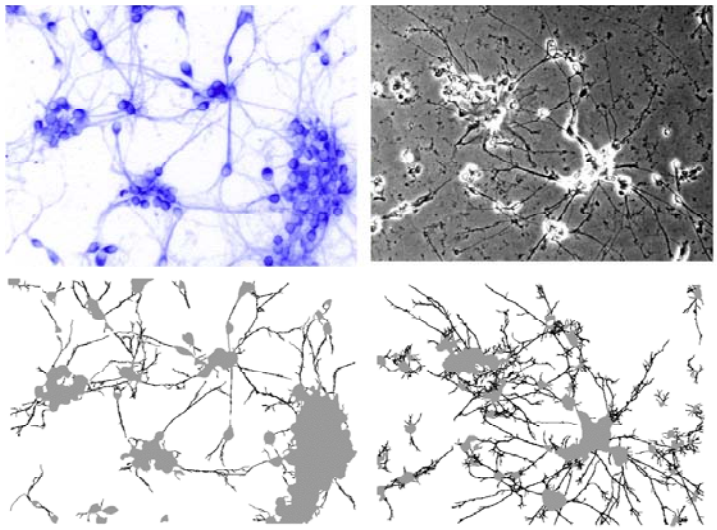

Figure 25. Digitized microscope images of both stained and non-stained neuron cell cultures treated with METH. Below the raw images are preliminary results of the modified algorithm as applied to each image.

Reference

1. Weaver, C. M., Pinezich, J. D., Lindquist, W. B. and Vazquez, M. E. An algorithm for neurite outgrowth reconstruction. Brain Research, submitted 2001.

4.4.3 Cardiac Electrophysiology

Sudden cardiac failure is a major cause of death. The causes and conditions leading to sudden cardiac death are complex and varied, and have been the subject of extensive studies. In collaboration with researchers from Hofstra University and Beth Israel Medical Center, we have been studying the dynamics of ventricular fibrillation, an irregular and chaotic heart rhythm that almost always results in sudden cardiac death.

We have been modeling cardiac electrophysiology through computer simulation. For this purpose it is common to use the monodomain equation which limits the electrical activity within cells. In reality, the ion-mediated current travels into and out of cells, requiring a bidomain model to more accurately simulate complex cardiac electrophysiology,

$$\begin{aligned} \frac{\partial_u}{\partial_t} &= \frac{1}{\chi C_m}\nabla\cdot\sigma_e\nabla u_e + \frac{f(u)}{R_m C_m} \\ \nabla\cdot\sigma_i\nabla u + \nabla\cdot\left(\sigma_i+\sigma_e\right)\nabla u_e &= 0 \end{aligned} \tag{1}$$

In the bidomain Equation (1), u_i and u_e are, respectively, intra and extra cellular potentials, $u = u_i - u_e$ is the transmembrane potential, F_i and F_e are conductivity tensors, and C_m, R_m, and O are the membrane capacitance, membrane resistance and surface-to-volume ratio. The reaction term f(u) represents the ionic current.

We developed a code to solve the bidomain equations. With this code, we will be able to study the onset of ventricular fibrillation and the dynamics of the ventricular fibrillation.

The study of the events leading to ventricular fibrillation involves a broad range of time scales from milliseconds to hours. The spatial detail required to understand this problem requires finely discretized meshes. This requires an efficient computer code in terms of memory and speed. Therefore, parallelization of the code is inevitable. We will use an ADI scheme to solve the 3-dimensional problem through the solution of a series of 1-dimensional problems employing a parallel tridiagonal solver from ScaLapack.

The simulations will be validated by comparison with experimental data, and the code will be used in a large-scale study of wave stability and scroll wave dynamics in realistic 3D anatomy. Large-scale simulations will provide critical insights into basic cardiac physics and dynamics. Moreover, the use of these models will allow experiments which cannot be performed with animal models because variability among individuals within a species makes it difficult to isolate causal factors.

References

1. Fenton, F. and Karma, A. Vortex dynamics in 3D continuous myocardium with fiber rotation: fibrillation. CHAOS **8**, 20 (1998).
2. Fenton, F., Evans, S., and Hastings, H.M. Memory in an excitable medium: A mechanism for spiral wave breakup in the low excitability limit. Phys. Rev. Lett. **83**, 3964-3967 (1999).
3. Hastings, H.M., Fenton, F., Evans, S., Hotomaroglu, O., Geetha, J., Gittelson, K., Nilson, J., and Garfinkel, A. Alternans and the onset of ventricular fibrillation. Phys Rev E **62**, 4043 - 4048 (2000).
4. Keener, J.P. and Bogar, K. A Numerical method for the solution of the bidomain equations in cardiac tissue. Chaos **8(1)**, 234-241.

4.5 ADVANCED SCIENTIFIC COMPUTING

See Table 7 for a list of projects.

TABLE 7. CDIC ADVANCED SCIENTIFIC COMPUTING PROJECTS

Project Title	Key Personnel	Comments
TSTT : Frontier-Lite	X. Li	Tech Transfer
Magnetohydrodynamics of Multifluid Systems	R. Samulyak, W. Oh, J. Glimm, J. Davenport	Multiple Applications
ViStA: Visual Statistical Analyzer	K. Mueller, W. Zhu, N. Volkow, D. Imre	Drug Abuse, Alzheimer's Disease, Aerosols in Climate
Uncertainty Quantification	J. Glimm	Decision Making
Visualization	K. Mueller, A. Peskin, M. McGuigan	Viz Theater
Cluster Computing	N. D'Imperio, E. McFadden	Cost Effective

4.5.1 TSTT: Frontier-Lite

The Front tracking code FronTier has achieved, in several cases, the first, and in some cases the only simulations to show agreement with laboratory experiment for acceleration-driven fluid mixing flows [1].

In Figure 26 (left frame) we display the interface between the light and heavy fluids for a gravity inverted mixing simulation at late time. In Figure 26 (right frame) we display the penetration distance of the light fluid bubbles into the heavy fluid plotted vs. the acceleration time scale Agt^2, where $A = (\rho_2 - \rho_1) / (\rho_2 + \rho_1)$, the Atwood number, is a dimensionless density ratio and g is the acceleration of gravity. The two curves correspond to two different initial conditions, with differing numbers of initial perturbations.

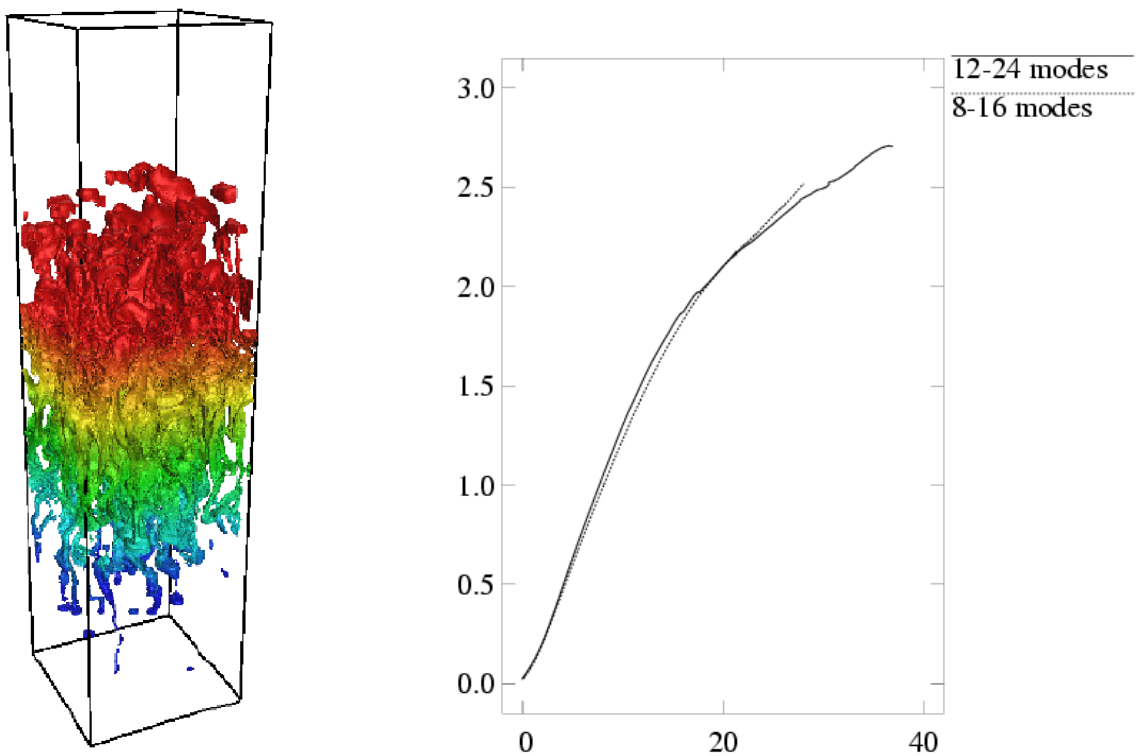

Fig. 26. Left: Interface between light and heavy fluids at late time in an acceleration driven mixing simulation. Right: Penetration distance of light fluid bubbles into the heavy fluid, as a function of Agt^2, $A = (\rho_1 - \rho_2) / (\rho_2 + \rho_1)$.

We have also determined the cause of the observed slow mixing rates for most simulations: numerical diffusion [1]. We have given a simple theoretical calculation based on the renormalization group and self similar scaling [2], which also gives mixing growth rates in agreement with experiment.

There is a growing interest in the transfer of the Front Tracking technology to other codes. We have largely completed the merge of FronTier with the AMR code Overture from LLNL. In Figure 27 we show the AMR refined patches and the tracked interface separating two fluids in distinct colors, for this combined code.

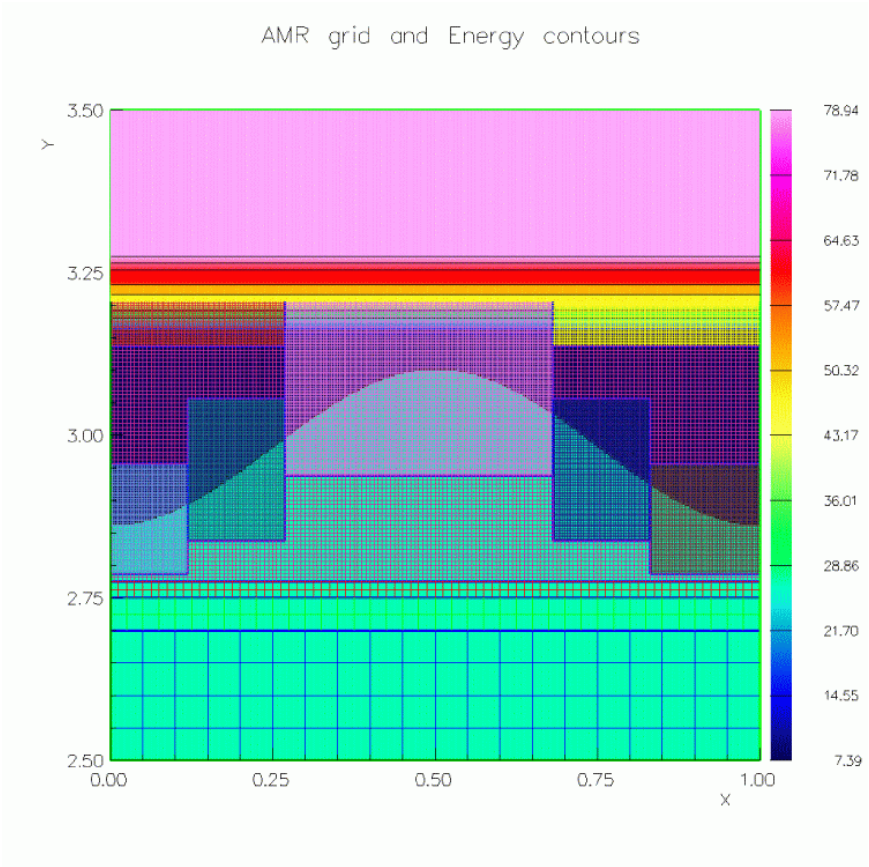

Figure 27. Shock-contact interaction, solved with combined FronTier (front tracking) and Overture (AMR) codes.

We are exploring the possibility of merging FronTier with the LANL code SAGE, and we will also combine FronTier with PNNL codes to model the dynamics of cells for biological studies.

To respond to this growing interest, we will develop a simplified version of the Front Tracking software, called FronTier-Lite, in the form of libraries which can be linked to other codes, and provide front tracking enhancements to them.

We have also improved the basic tracking algorithm. In a still experimental development [3, 4, 5], we have developed a new tracking algorithm, based on the tracking of an interface in both space and time. This method simplifies the differencing associated with tracking and transfers most of the difficulty to the computational geometry of a description of the moving interface. The result is now fully conservative, even at the tracked front, and it gains one order of accuracy in its rate of convergence. For these two reasons, the new algorithm is a very promising development.

References

1. George, E., Glimm, J., Li, X.-L., Marchese, A., and Xu, Z.L. A comparison of experimental, theoretical and numerical simulation Rayleigh-Taylor missing rates. Proc. Nat. Acad. Sci. **99**, 2581-2592 (2002).
2. Cheng, B., Glimm, J., and Sharp, D.H. A 3D RNG bubble merger model for Rayleigh-Taylor mixing. Chaos **12**, 267-274 (2002).
3. Glimm, J., Li, X.-L., and Liu, Y.-J. Conservative front tracking in one space dimension. Contemporary Mathematics. To appear.
4. Glimm, J., Li, X.-L., Liu, Y.-J., and Zhao, N. Conservative front tracking and level set algorithms. Proc. Nat. Acad. Sci. **98**, 14198-14201 (2001).
5. Glimm, J., Li, X.-L., Liu, Y.-J., and Xu, Z. Conservative front tracking with improved accuracy. SIAM J. Num. Anal. Submitted.

4.5.2 Magnetohydrodynamics of Multifluid Systems

Introduction. During the last decades, magnetohydrodynamics of conducting fluids has achieved significant theoretical and experimental results (see [8,9,10] and references therein). Despite this progress, there are still unresolved questions, as well as a remaining need for highly resolved, large-scale numerical simulations of free surface MHD flows. This project aims to fill partially a gap between experimental and computational studies of free surface MHD flows in conducting fluids.

The system of equations for free surface MHD flows is a coupled hyperbolic-parabolic/elliptic system in a geometrically complex moving domain. The development of numerical methods and computational software requires scalable parallelized algorithms for elliptic and parabolic equations in three dimensions with strong, geometrically complex discontinuities in the coefficient matrix defining the Laplacian operator. The numerical algorithms are implemented as a magnetohydrodynamics extension of the FronTier code. FronTier, a hydrodynamics code with free interface support, is based on front tracking, a numerical method that allows the computation of dynamically evolving interfaces. The method is able to detect and resolve changes in the topology of the moving front. It allows reduction in the level of grid refinement and has no interfacial numerical diffusion. The method of front tracking is ideal for problems with strong discontinuities. We implemented in the FronTier-MHD code a grid moving algorithm, to bring distorted, but logically rectangular, grid elements into alignment with discontinuity surfaces, so that no discontinuity crosses a finite element boundary. This algorithm requires a high level of topological robustness in its interface handling, including intersection detection and interface topology determination, which are issues basic to computational geometry. The grid is used for finite element elliptic and parabolic solvers of the magnetic field, and current density evolution equations based on Raviart-Thomas and vector Whitney elements.

Such a code will satisfy the need for high-performance computing in scientific and engineering studies of MHD processes for several challenging DOE projects. Global numerical simulation of the muon collider target is the most important current application for our code. The target will be designed as a pulsed jet of mercury interacting in a strong magnetic field with high-energy proton

beams. Global numerical simulations of hydro- and magnetohydrodynamic processes in such a target can resolve many important engineering design problems and reduce the number of costly experiments. The lack of high-quality numerical simulations of the liquid target for the Spallation Neutron Source project was one of the major reasons that led to the failure of the liquid target project. Other applications include the simulation of various liquid metal flow regimes in the Tokamak cooling system and modeling MHD processes in experiments with exploding wires. Our research also aims to study numerically some fundamental questions arising in free surface MHD flows, such as the stability and breakup of jets, processes involving droplets, and cavitation of liquid metals.

Numerical modeling of the behavior of MHD flows under extreme thermodynamics conditions is among our major research goals. The achievement of high-quality, numerical simulations of such problems relies on accurate modeling of thermodynamic properties of fluids. For this purpose, we have developed a theoretical model and a FronTier software library for an analytic isentropic two-phase equation of state describing the liquid-vapor phase transition. This equation of state is applicable for studying cavitation processes in liquids. We will develop a general (non-isentropic), two-phase, EOS model for the study of processes that goes beyond the adiabatic approximation. We will also use the SESAME EOS library in cases for which such a highly accurate EOS is required.

Mathematical formulation. The system of equations governing a compressible inviscid conducting fluid in a magnetic field is

$$\frac{\partial \rho}{\partial t} = -\nabla \cdot (\rho u)$$

$$\rho\left(\frac{\partial}{\partial t} + \mathbf{u}\cdot\nabla\right)\mathbf{u} = -\nabla P + \rho\mathbf{g} + \frac{1}{c}(\mathbf{J}\times\mathbf{B})$$

$$\rho\left(\frac{\partial}{\partial t} + \mathbf{u}\cdot\nabla\right)e = -P\nabla\cdot\mathbf{u} + \rho\mathbf{u}\cdot\mathbf{g} + \frac{1}{\sigma}\mathbf{J}^2$$

$$\frac{\partial \mathbf{B}}{\partial t} = \nabla\times(\mathbf{u}\times\mathbf{B}) - \nabla\times\left(\frac{c^2}{4\pi\sigma}\nabla\times\mathbf{B}\right)$$

$$\nabla\cdot\mathbf{B} = 0,$$

where ρ, $\mathbf{u}$, P, and e are the fluid density, velocity, pressure, and the specific internal energy of the fluid, correspondingly, $\mathbf{g}$ is the gravitational acceleration, B is the magnetic field induction and J is the current density distribution. This system must be completed by an appropriate equation of state. The following boundary conditions:

$$\mathbf{n}\cdot(\mathbf{B}_2 - \mathbf{B}_1) = 0,$$

$$\mathbf{n}\times(\mathbf{H}_2 - \mathbf{H}_1) = \frac{4\pi}{c}\mathbf{K},$$

must be satisfied at the free fluid interface, where $\mathbf{B} = \mu \mathbf{H}$, μ is the magnetic permeability and **K** is the surface current density which is zero for finite conductivity fluids. The MHD system is solved using the operator splitting technique.

In many important physics applications, the influence of eddy currents on the external magnetic field can be neglected and the current density distribution can be found by solving the Poisson equation

$$\mathbf{J} = \sigma\left(\nabla\phi + \frac{1}{c}\mathbf{u}\times\mathbf{B}\right)$$

$$\Delta\phi = -\frac{1}{c}\nabla\cdot(\mathbf{u}\times\mathbf{B}),$$

$$\text{with } \left.\frac{\partial\phi}{\partial\mathbf{n}}\right|_{\Gamma} = -\frac{1}{c}(\mathbf{u}\times\mathbf{B})\cdot\mathbf{n}$$

The MHD equations represent in this case a coupled hyperbolic – elliptic system.

Numerical implementation. The coupling of elliptic/parabolic systems to hyperbolic systems, which arises in the mathematical formulation of the MHD problem, is solved using operator splitting. The hyperbolic system of the MHD equations is solved on a finite difference grid in both domains separated by the free surface using FronTier's interface tracking numerical techniques. The evolution of the free fluid surface is obtained through the solution of the Riemann problem for compressible fluids. The elliptic equation for the current density distribution is solved using a finite element method based on Raviart-Thomas elements. We have been working on the parabolic solver for the magnetic field evolution equation using Whitney vector finite elements. The tetrahedral finite element grid is rebuilt at every time step and conformed to the new shape and position of the dynamically evolving interface. This is accomplished by using a point-shifted grid which conforms to the tracked interface, and which has a rectangular index structure. Scalable parallelism will use direct methods to solve the elliptic/parabolic term on each processor, and a wire basket outer iteration to ensure matching conditions across processor domain boundaries.

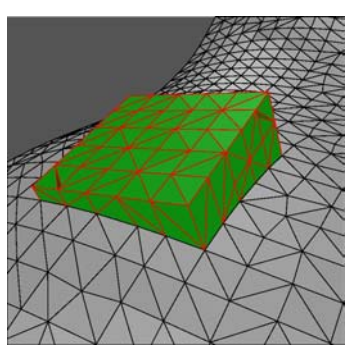

Figure 28. Triangulated tracked surface and tetrahedralized hexahedra conforming to the surface. For clarity, only a limited number of hexahedra have been displayed.

Results of numerical simulation. As an example of the numerical simulation using FronTier-MHD code, we present results of the study of Richtmyer-Meshkov instability in conducting liquid jets due to an external energy deposition. This problem arises as part of the design of the target for a proposed high energy accelerator, the Muon Collider (see [7,11] and Section 4.2.1 of this document). The target will be designed as a pulsed jet of mercury interacting with strong proton pulses in a 20 Tesla magnetic field. Without a magnetic field, shock waves due to the deposition of proton energy lead to strong Richtmyer-Meshkov type instabilities of the jet surface and the jet breakup. A strong axial magnetic field significantly reduces the amplitude and velocity of surface instabilities and shock waves (see Figure 29).

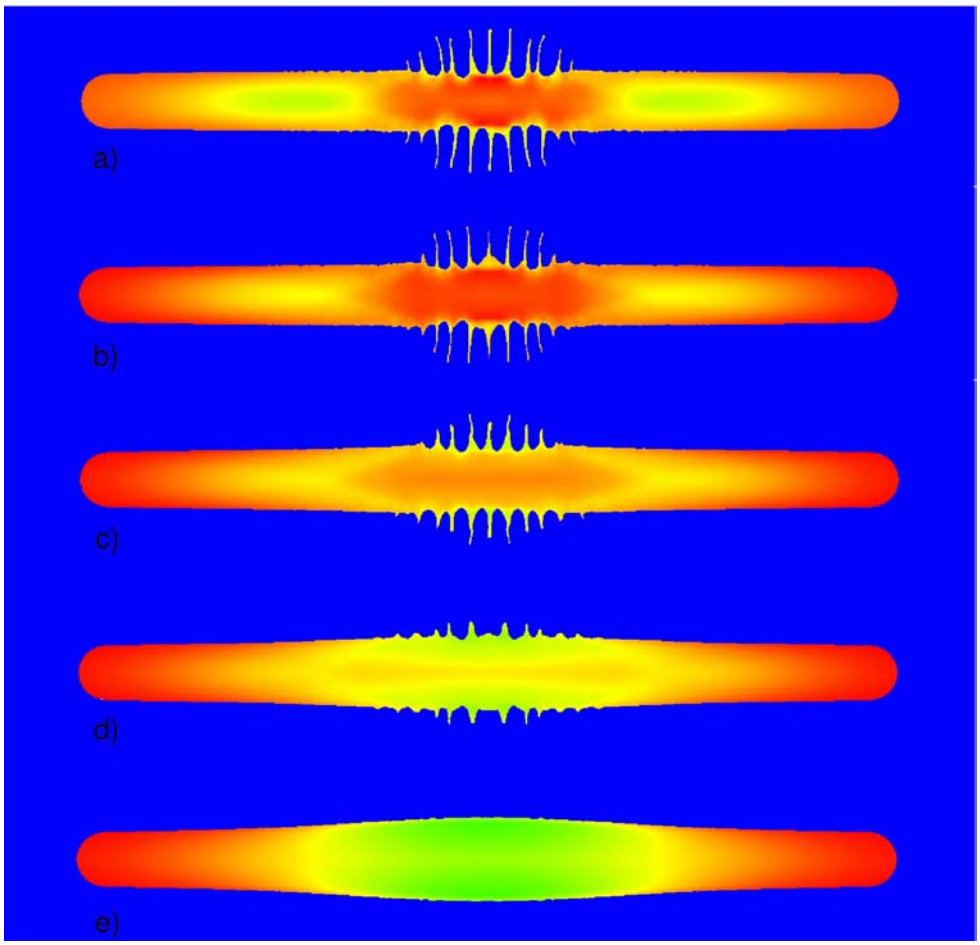

Figure 29. Richtmyer-Meshkov instability in MHD jet due to external energy deposition. Stabilizing of the mercury jet by the longitudinal magnetic field: a) B=0, b) B = 2T, c) B = 4T, d) B = 6T, e) B = 10T.

Other applications will include the modeling of free surface lithium flows in a proposed Tokamak cooling system, and the dynamics of melted metal jets in experiments with exploding wires.

References

1. Landau, L.D. and Lifshitz, E.M. *Electrodynamics of Continuous Media*. Addison-Wesley Publishing Co., Reading, MA, 1960.
2. S. Chandrasekhar, S. *Hydrodynamic and Hydrodynamic Stability.* Clarendon Press, Oxford, 1961.
3. Glimm, J., Grove, J.W., Li, X.L., Shyue, K.M., Zhang, Q., and Zeng, Y. Three dimensional front tracking. SIAM J. Sci. Comp. **19**, 703-727 (1998).
4. Glowinski, R. and Wheeler, M. Domain decomposition and mixed finite element methods for elliptic problems. In R. Glowinski, G. Golub, G. Meurant, and J. Periaux, Eds., *Proceedings of the First International Symposium on Domain Decomposition Methods for Partial Differential Equations,* pp. 144-172. SIAM, Philadelphia, 1988.
5. Chan, T.F. and Mathew, T.P. Domain Decomposition Algorithms. Acta Numerica **3,** 61-14 (1994).
6. Cowsar, L.C., Mandel, J., and Wheeler, M.F. Balancing domain decompositions for mixed finite elements. Math. Comput. **64**, 989-1015 (1995).
7. Ozaki, S., Palmer, R., Zisman, M., and Gallardo, J., Editors. *Feasibility Study-II of a Muon-Based Neutrino Source.* BNL-52623, June 2001; available at http://www.cap.bnl.gov/mumu/studyii/FS2-report.html
8. Molokov, S. and Reed, C.B. Review of free-surface MHD experiments and modeling. Technical Report ANL/TD/TM99-08, Argonne National Laboratory (1999).
9. Morley, N., Smolentsev, S., Barleon, L., and Kirillov, I. Liquid magnetohydrodynamics - recent progress and future directions for fusion. Fusion Engineering and Design, **51-52,** 701-713 (2000).
10. Oshima, S., Yamane, R., Mochimaru, Y., and Matsuoka, T. The shape of a liquid metal jet under a non-uniform magnetic field. JSME Int. J. **30**, 437-448 (1987).
11. Samulyak, R. Numerical simulation of hydro- and magnetohydrodynamic processes in the Muon Collider target. Lecture Notes in Comp. Sci. **2331**, 391-400 (2002).

4.5.3 ViStA: Visual Statistical Analyzer

Today's ubiquitous data collection devices and procedures amass huge amounts of data in relatively small durations of time. We are thus faced with the daunting task of extracting the relevant information from the resulting data sets. The datasets are often comprised of data points with enormous attribute sets, creating a very high-dimensional exploration space, including the dimension of time. For example, one of our domain applications is the classification and survey of aerosol particles, acquired by a highly sensitive single-particle mass spectrometer that has recently been developed at BNL. Here, each mass spectrum data vector is composed of 250 bins, a typical data collection is at the order of terabytes, and the task is to categorize the collected aerosols such that inferences on their origin as well as their impact on the environment can be drawn. Another of our domain applications is based in the field of cancer research-motivated proteomics, where we are seeking to identify cancer-correlated protein patterns in blood samples. In this case, the mass spectra vector associated with the proteins has 150,000 bins, which amounts to an even larger data space than in the aerosol application. Yet another domain application of ours is that of human brain mapping, where neuro-scientists collect vast amounts of data via functional imaging methods,

such as fMRI and PET, in their quest to figure out the web of connectivity in the human brain. Given the complexity of the matter at hand, this task is one of the most daunting of all.

To tackle these challenging applications, we are currently developing ViStA (the Visual Statistical Analyzer), a framework for the interactive exploration and mining of large multi-variate data collections. ViStA couples effective and efficient statistical routines with a powerful interactive multi-tier information visualization surface, and is designed to form the support structure for many different types of data mining tasks. ViStA employs a statistics engine that produces a first organizational model of the data, which the user may explore at will, using the multi-modal visual interface. The user could subsequently postulate a model hypothesis, which can be tested by ViStA's statistics engine. The user can also re-model part of the data and ViStA will then update the modeling of the entire data set using a Bayesian statistical framework.

ViStA is being developed within two quite diverse application scenarios, yet both resulting in data with very high-dimensional feature vectors: The mining and classification of large collections of high-dimensional mass spectra vectors, and the mining and exploration of causal relationships in functional brain data acquired from many individuals subjected to a great array of experimental conditions and tasks. Both give rise to a graph-like data organization: The former yields a hierarchical data organization in form of a tree, while the latter yields a directed graph. Statistical analysis drives the construction of these data organizations, and visualization conveys the complex relationships to the user. In the following, we describe the two subsystems of ViStA: SpectrumMiner and BrainMiner.

Evolution of Atmospheric Aerosols

Introduction. The purpose of this project is to develop data processing tools for the classification and time series analysis of atmospheric aerosol particles. Atmospheric aerosols play an important role in both climate and public health. Current research is focused on determining the chemical composition of aerosols, and thus the composition of air and its evolution over time. Massive mass spectra data, on the scale of terabytes per week, have been collected continuously over time by researchers in the Atmospheric Sciences Division at Brookhaven using their cutting-edge, field deployable high precision mass spectrometer. Our first task is to determine the chemical composition of each aerosol based on its mass spectrum. Subsequently, we classify aerosols by their chemical compositions and thus determine the air composition at each time point. Finally, we study the time series evolution of atmospheric compositions identifying normal as well as abnormal patterns in real time.

To convey the analysis results to the scientists in an intuitive way and to incorporate their expert knowledge into the data analysis phase, an interactive graphical user interface utilizing modern scientific visualization techniques becomes a necessity. Large-scale BNL data collections have reached sizes for which straightforward visualization techniques are starting to fail. In this spirit, our proposed approach couples a powerful Bayesian classification and multivariate time series analysis engine with an intuitive and responsive graphical user interface to fine-tune the underlying models.

The Statistics Engine. We first classify aerosols based on their mass spectra through an iteration of expert-machine interaction using a Bayesian classifier. The Bayesian classifier can incorporate not only explicit classification rules but also prior knowledge in terms of a partial training data set. We have also been implementing automatic procedures to elucidate the structure of the compounds. To study the evolution of aerosols and the changes in atmospheric composition versus time, both the univariate and the multivariate time series analyses are employed to unravel trends and patterns.

The traditional statistical classifier would take only explicit classification rules. Machine learning techniques such as the neural network would take only a training set. However, the semi-supervised clustering approach we are taking requires the classifier to learn from both the explicit rules and the implicit rules embedded in a partial training set established by the expert as they survey the current clustering results and make adjustments to the clusters. For this we have implemented a Bayesian classification framework that could absorb the up-to-date prior information in both the explicit and implicit formats, and produce the updated posterior classification results.

For efficient classification and automatic structure elucidation, we have been constructing a molecule library where the signature profile and class membership of each molecule is established. The molecules are classified along a natural chemical classification tree with two categories--organic and inorganic--at the initial node. Subsequently, the organics are further divided into classes of carboxylic acids, aldehydes, ketones, alkenes, alkanes, aromatics, etc. We begin with the spectra of known molecules (NIST library or lab-generated).

Visualization. SpectrumMiner provides a highly visual interface for the interactive mining, survey, and classification of these large, high-dimensional data collections. SpectrumMiner's hierarchical classification algorithm is user-steerable via a novel visual interface, which we call the *interactive dendogram* [1]. Hierarchy nodes are placed on concentric circles whose radii are determined by the dissimilarity of the node's sub-tree. We chose a circular layout of the dendogram since it makes better use of space than its linear counterpart. It inherently dedicates less drawing space to the higher-level, less numerous nodes, and distributes more space to the many leaf nodes along the circumference of the circle. In Figure 31, we show a screen capture of SpectrumMiner, with the interactive dendogram located on the bottom right. Edges are colored using a rainbow colormap to indicate the number of data items they carry. Above the dendogram is the 4D time-slice selector. The interactive dendogram represents time-varying data as a cylindrical shape composed of a stack of circular time-slice dendograms. The time-slice selector shows the unwrapped outer surface of this cylinder, with each horizontal slice capturing the leaf nodes of one time-slice dendogram. Patterns in the data distribution over time are clearly visible. Stepping across the time slices will animate the data-related coloring of the dendogram's arcs. To the left of the dendogram is the node viewer. Selecting a particular node will display the average spectrum of all data items classified into the node (window with white background), as well as the node's data composition (window with blue background just below).

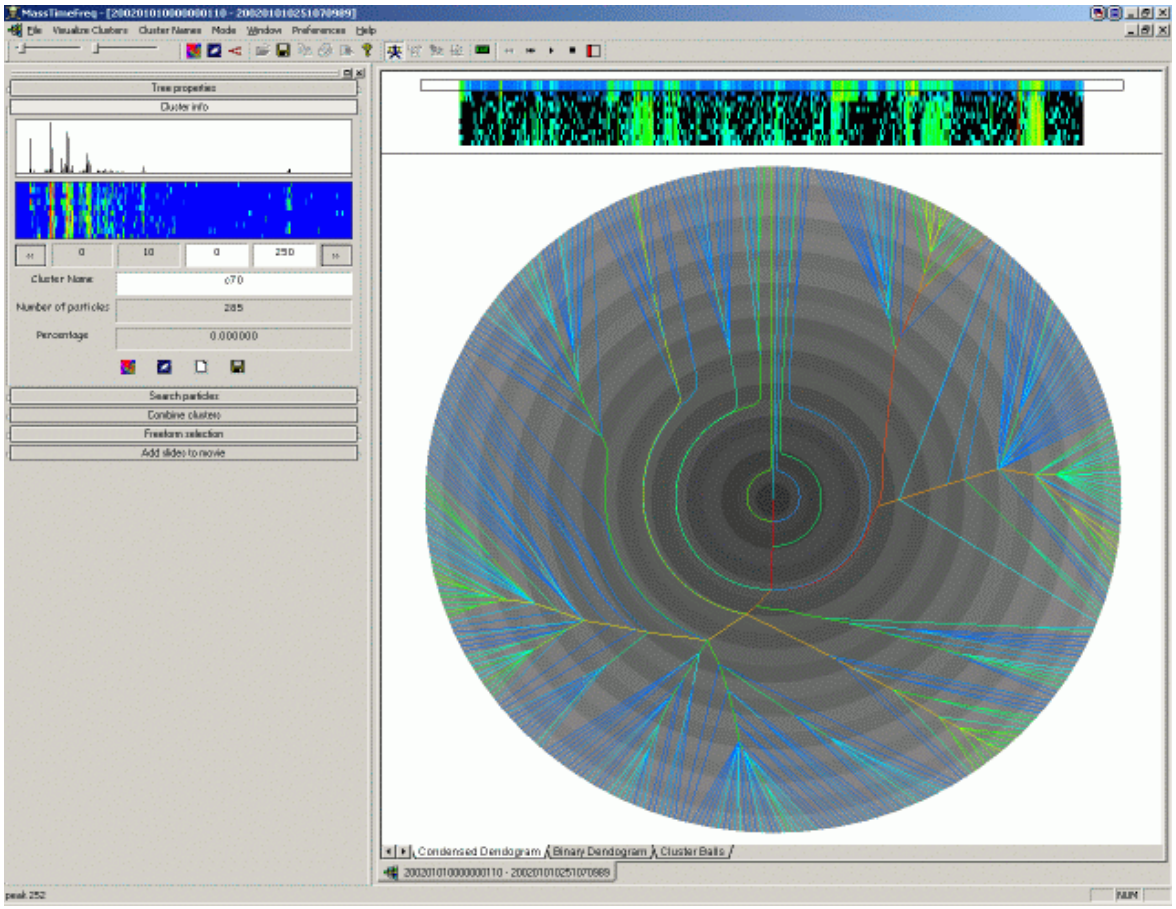

Figure 31. SpectrumMiner's interactive dendogram interface.

Analysis and Visualization of Human Brain Function

Overview. A major goal of statistical analysis in brain research is to extract from a vast amount of brain image data (PET and fMRI) the essential features that characterize brain functions. We are developing two novel approaches for such analysis: (1) Correlational and Path Analysis to uncover brain functional networks, and (2) coefficient of variation (CV) -- a measure of brain regional variability or heterogeneity. These analyses are being implemented in BrainMiner, an interactive brain functional analysis and visualization tool [9, 10, 13].

Correlational and Path Analysis. The correlations in brain activity are calculated on the basis of predefined anatomical regions-of-interest (ROIs). The correlation coefficient is then employed to quantify similarity in response, for various regions during an experimental setting. To account for anatomical variability, each test subject's volumetric brain data is first transformed into a common anatomical coordinate system (the Talairach-Tournoux space). Statistical analyses of brain functional relationships include:

1. The correlational analyses, including the Pearson product-moment correlations, the partial correlations and the canonical correlations.
2. Cluster analysis.

3. Principal component analysis (PCA) and the factor analysis (FA).
4. Path analysis and time series analysis.

Measuring Brain Functional Variability. It is well known that the two most essential statistics are mean and variance. In ROI-based brain functional studies, the analysis of the regional mean is a fully developed practice; however, the same is not true for the variability. We have developed the analysis for brain functional homogeneity/heterogeneity based on the coefficient of variation (CV). The CV is the ratio of the standard deviation to the mean. It is a measure of regional variability independent of the underlying measurement unit. We have applied such analysis to the comparison of brains affected by Alzheimer's disease (AD) with normal ones [10]. Our results indicate that such analysis is providing new insight into disease etiology and additional information on diagnosis.

The amount of statistical data can be enormous, and effective tools are essential if the brain researcher is to grasp and discover functional relationships quickly from the statistical data. BrainMiner has a powerful visualization tool that facilitates this task [8–13].

Viewing in 3D. We have developed a 3D visualization interface that displays correlational data for each ROI, along with an MRI volume and a digitized version of the Talairach atlas. Both can be sliced in three orthogonal directions and can be overlaid on each other. A basic view with a few ROIs is shown in Figure 32, which shows the Graphical User Interface (GUI) of our newly developed 3D brain visualization software, along with a basic view of a small number of ROIs embedded into a cut-out area of a normalized/standardized MRI brain. Similar to the 2D viewer, the colors of the ROIs denote the strength of the correlational relationship, on a rainbow scale. The root ROI is colored in yellow. The GUI allows the user to slide the cutting planes up and down and back and forth, to rotate the volume, and to select certain brain surfaces, such as white matter, gray matter, and skull, to be semi-transparently superimposed. The correlation thresholds can also be selected, and many more features are available.

The number of ROIs to be displayed, however, can become quite large (about 120-140), which poses challenging problems in the visualization task: in a space too crowded with statistically significant ROIs, it becomes very hard, if not impossible, for the user to tell the 3D positions of the individual ROIs. To overcome these difficulties, a number of techniques [2-8] were investigated:

- Superimposing a Talairach atlas slice that can be slid up and down the volume.
- A single light source placed above the volume in a fixed position, providing specular lighting cues for the height and depth of each ROI sphere (this can be seen in Figure 32).
- Enhancing the ROIs by colored halos, where the colors code their height and depth on a rainbow color scheme. The ROIs are connected by iso-lines to the MRI volume cuts, which suggests their position in 3D space.
- Projecting a colored grid onto the volume cuts, again encoding height and depth on a rainbow map. Colored shadows cast onto the exposed volume slices provide additional cues.
- Projecting the ROIs onto the brain iso-surface, such as white or gray matter, or skin.
- Grouping ROI networks into composite polygonal objects, which reduces the object complexity of the scene.

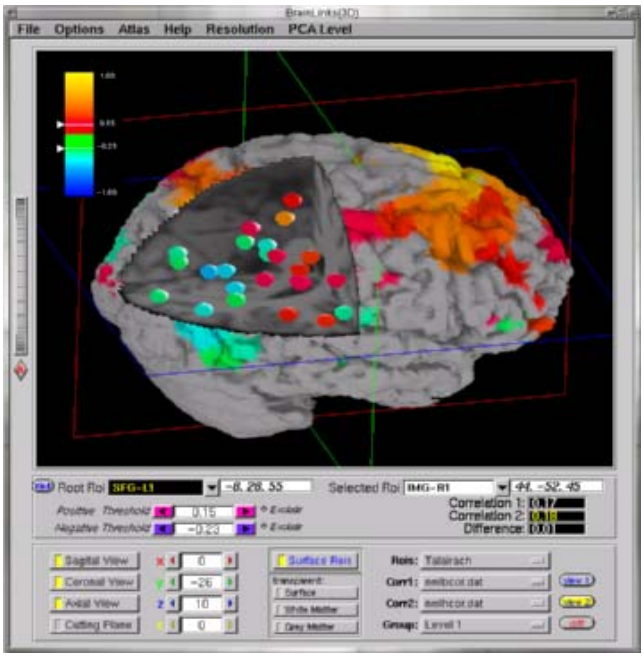

Figure 32**.** GUI for 3D brain visualization software.

Results. We are continuing our effort towards the discovery of brain functional networks. Intriguing results on brain functional homogeneity/heterogeneity have already been obtained. In analyzing the PET images of 35 subjects with AD and 35 age and gender matched healthy controls, we found that AD subjects showed a significantly larger CV for the whole cortex but had a significantly greater number of regions with increased homogeneity (decreased CV) than the controls. At the regional level the reductions in CV in the AD subjects were associated with reductions in metabolism that were most accentuated in the parieto-temporal cortex, except for the precuneus, which had a marked reduction in metabolism but increased CV. Discriminant analyses showed that the combination of variables that best discriminated between AD and controls were metabolism and CV in left parietal, CV in right precuneus and global CV (94% sensitivity and 100% specificity) [10]. BrainMiner allows many types of interactive explorations of brain functional image data. It is currently used by a number of brain researchers and is being refined continuously.

It is well known that once the data become too large in size and/or dimensionality, automated data mining approaches begin to fail. To address these shortcomings, our current efforts target a classify-refine mechanism that inserts the scientist into a tight loop in the data mining process. In this new extension to ViStA, the user may re-organize or re-structure certain parts of the model or data portions directly on the visual display surface. The changes in the data organization or model are promptly recognized by the statistics engine, which then performs the necessary parameter adjustment/tuning to reflect the changes made by the user. Subsequently, a new data organization or model is computed and presented visually to the user, who may then opt to begin a new iteration cycle.

References

1. Imrich, P., Mugno, R., Mueller, K., Imre, D., Zelenyuk, A., and Zhu, W. Interactive poster: Visual data mining with the interactive dendogram. To be presented at the Information Visualization Symposium, 2002.
2 Meissner, M., Huang, J., Bartz, D., Mueller, K., and Crawfis, R. A practical comparison of popular volume rendering algorithms. *2000 Symposium on Volume Rendering*, pp. 81-90, Salt Lake City, October 2000.
3. Mueller, K., Shareef, N., Huang, J., and Crawfis, R. High-quality splatting on rectilinear grids with efficient culling of occluded voxels. IEEE Trans. Vis. and Comp. Graph. **5(2)**, 116-134 (1999).
4. Mueller, K., M`ller, T., Swan, J.E., Crawfis, R., Shareef, N., and Yagel, R. Splatting errors and antialiasing. IEEE Trans. Vis. and Comp. Graph. **4(2)**, 178-191 (1998).
5. Levoy, M. Efficient ray tracing of volume data. Acm Trans. Comp. Graph. **9(3)**, 245-261 (1990).
6. Kaufman, A. *Volume Visualization*. IEEE Computer Society Press, Los Alamitos, CA, 1991.
7. Fruchterman, T. and Reingold, E. Graph drawing by force-directed placement. Software-Practice and Experience **21(11)**, 1129-1164 (1991).
8. Meade, J., Zhu, W., Mueller, K., Welsh, T., and Volkow, N. Brain Tableau – the 2D brain functional visualization & analysis software. Medical Imaging 2001, 17-23 February, San Diego, CA.
9. Mueller, K., Welsh, T., Zhu, W., Meade, J., and Volkow, N. Brain Miner: A Visualization Tool for ROI-Based Discovery of Functional Relationships in the Human Brain, *New Paradigms in Information Visualization and Manipulation (NPIVM) 2000*, Washington DC, November 2000.
10. Volkow, N., Zhu, W., Felder, C., Mueller, K., Welsh, T., Wang, G.-J., and De Leon, M. Changes in brain functional homogeneity in subjects with Alzheimer's disease. J. Psychiatry Research: Neuron Imaging **114(1)**, 39-50 (2002).
11. Welsh, T., Mueller, K., Zhu, W., Meade, J., and Volkow, N. Brain Explorer– the 3D brain functional visualization & analysis software. Medical Imaging 2001, 17-23 February, San Diego, CA.
12. Welsh, T., Mueller, K., Zhu, W., Volkow, N., and Meade, J. Graphical strategies to convey functional relationships in the human brain: A case study. *Visualization '01*, pp. 481-485, San Diego, October 2001.
13. Zhu, W., Volkow, N., Mueller, K., Welsh, T., and Meade, J. BrainMiner – An interactive tool for brain functional connectivity study. Human Brain Mapping 2001, Brighton, England, June 2001.

4.5.4 Uncertainty Quantification

Quantification of Uncertainty and Computer Assisted Decision Making

The need for computer assisted decision making is driven by two related factors. The first is the importance of complex scientific/technical decisions, such as those related to global warming, for which controlled experiments are not feasible. The second is the need for rapid or timely decisions,

using incomplete information, such as in shortening the time to market duration of a product design cycle, mandating a reduction of the role of the human in the loop.

The result is a strong increase in the requirement of fidelity in physical, mathematical, and computer-based models of reality. Also required, and the focus of the work being conducted here, is a measurement of accuracy, or error inherent in model prediction [1]. Assessment of errors has three uses: (1) to allow refinement of the model, in conjunction with observational data; (2) to quantify risk associated with model based predictions; and (3) to refine the simulation adaptively to reduce the error.

Uncertainty in prediction is measured in terms of confidence intervals, and these are proportional to the standard deviation, σ. We showed that σ, that is, uncertainty, from two distinct sources can be combined according to the standard RMS rule $\sigma^2 = \sigma_1^2 + \sigma_2^2$ [2]. Here σ_1 is a standard deviation associated with data (insufficiency of data or its uncertainty) and σ_2 is a standard deviation associated with simulation (simulation error, under resolution). Many of our studies were conducted in the context of petroleum reservoir engineering, in collaboration with Chevron, BP, LANL and Stony Brook University. We found a simple Gaussian model for the mean and the covariance of the solution error. Dependence of the model on grid parameters, geostatistical parameters and petroleum parameters was determined. Due to simplifications in the statistical model, a third contribution, σ_3^2 should be added to σ^2 , associated with statistical modeling errors for the choice of mean and covariance.

Continuing with the shock physics [3] studies, we are presently developing a composition law to combine errors from simple problems (wave interactions). We want to compose them to obtain the errors which arise in more complex problems. This step is important. The resources to solve complex problems will severely limit the extent to which the errors can be studied directly. In fact, study of error requires a statistical ensemble of still more accurate solutions, so that the errors in the original solutions can be observed directly. This will take us toward our goal of transferability, so that error models can be developed in a simple context and used, with only modest further tuning, in a complex situation.

References

1. Glimm, J., Lee, Y. H., and Ye, K. A simple model for scale up error. Contemporary Mathematics. Accepted for publication (2002).
2. Glimm, J., Hou, S., Lee, Y.-H., Sharp, D.H., and Ye, K. Solution error models for uncertainty quantification. Contemporary Mathematics. Submitted.
3. De Volder, B., Glimm, J., Grove, J.W., Kang, Y., Lee, Y., Pao, K., Sharp, D.H., and Ye, K. Uncertainty quantification for multiscale simulations. J. Fluids Engineering **124**, 29-41 (2002). LANL Report No. LA-UR-01-4022.

4.5.6 Visualization

Klaus Mueller, a faculty member of the Visualization Laboratory, is developing efficient volume rendering algorithms for interactive visualization of large datasets occurring in science, medicine, engineering, and entertainment (http://www.cs.sunysb.edu/~mueller).

One current area of interest is point-based volume and surface rendering. Here, we are seeking to exploit state-of-the-art commodity graphics hardware, in conjunction with rendering optimizations, such as smart volume encoding and occlusion culling, to render large 3D and 4D datasets at high quality and speed. 4D datasets, such as time-varying datasets, usually come on 4D Cartesian Cubic (CC) grids. In recent research, we explore the use of 4D Body Centered Cubic (BCC) grids to provide a more efficient sampling lattice. We use this lattice in conjunction with a point-based renderer that further reduces the data into an RLE-encoded list of relevant points. We achieve compression ranging from 50-80% in our experiments. Our 4D visualization approach follows the hyperslice paradigm: the user first specifies a 4D slice to extract a 3D volume, which is then viewed using a regular point-based full volume renderer. The slicing of a 4D BCC volume yields a 3D BCC volume, which theoretically has 70% of the datapoints of an equivalent CC volume. We reach compressions close to this in practice. The visual quality of the rendered BCC volume is virtually identical with that obtained from the equivalent CC volume, at 70-80% of the CC grid rendering time. The images below show a 4D turbulent jet dataset, hyper-sliced along various axes and volume rendered in 3D.

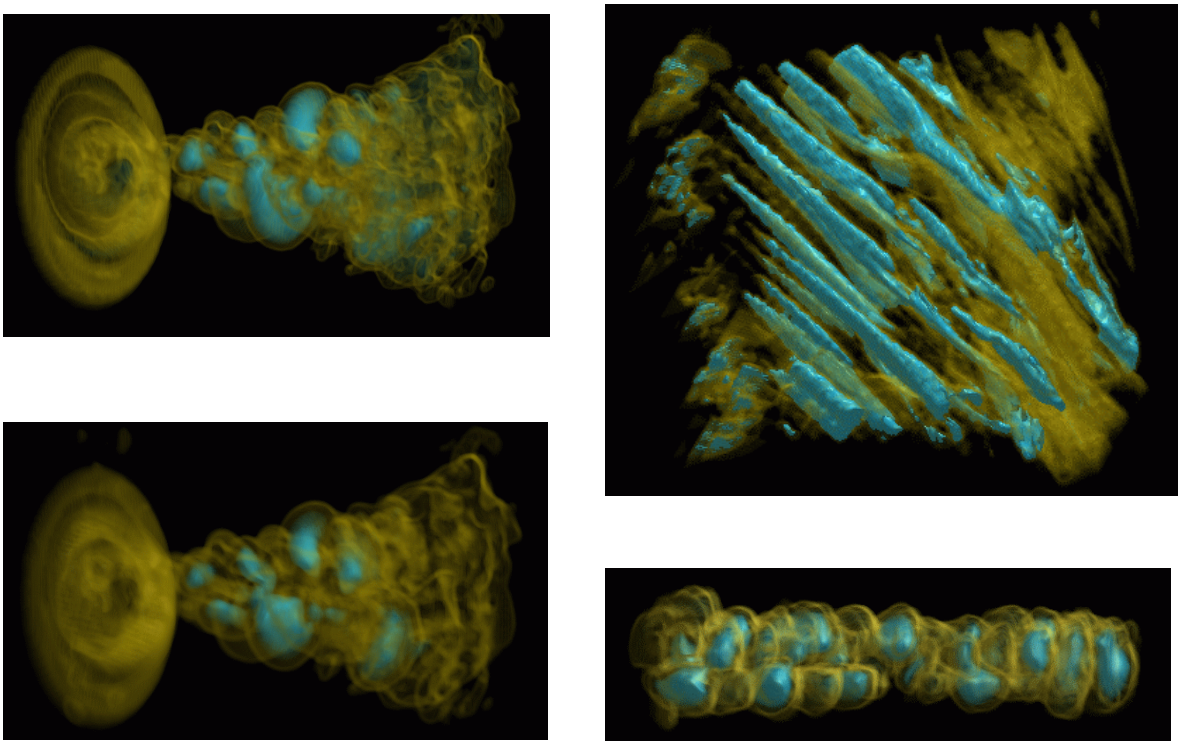

Figure 33. 4D turbulent jet dataset. Top left : 4D CC grid ; bottom left : 4D BCC grid; top right: hyperslice at z=62; bottom right: hyperslice at x=35.

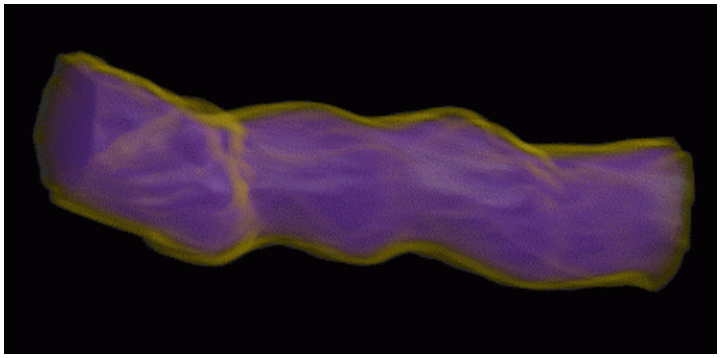

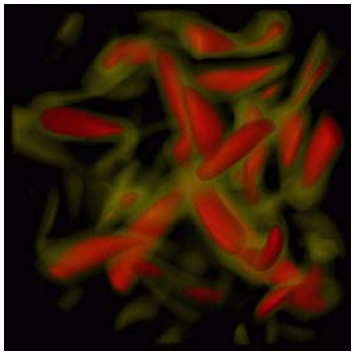

Figure 34. Left: A time instance of a time-varying jet shockwave dataset rendered with points; Right: A time instance of a turbulent flow dataset rendered with point-primitives.

In another line of research on point-based representations, we explore methods for converting an image or volume sampled on a regular grid into an irregular point hierarchy. The conversion process retains the original frequency characteristics of the dataset while providing a reduced number of points. First, we determine the local frequency characteristics of the source dataset at different scales. Then, we analyze this scale-space representation of the object to construct a hierarchy of points of different extents and coefficients. Finally, this hierarchy is traversed during image synthesis to identify the reduced set of points that still can represent local object detail, or satisfy some user-controlled threshold. Using an implementation of our approach, we were able to obtain a point reduction of up to an order of magnitude for images and up to one fourth for volumes. We have found that the images reconstructed even from a greatly reduced point set still maintain a high level of quality. The fundamental approach is particularly attractive for splat-based volume renderers, as their rendering complexity is directly related to the number of points in the dataset. To prove the concept, we have modified an existing splatting algorithm to render variable-sized points, and we were able to generate high-quality renderings, even for greatly reduced point sets.

4.5.5 Cluster Computing

Linux clusters have become important providers of computing cycles in the scientific world. Ours is modeled on similar clusters at Stony Brook (http://galaxy.ams.sunysb.edu/) and at BNL (http://www.ccd.bnl.gov/bcf/cluster/). It consists of 156 Intel Pentium III processors running at speeds from 500MHz to 1 GHz. Arranged in dual processor nodes, most have 1 Gbyte of memory per node. They are connected with a 100 Mbit/sec Cisco switch. A storage device with 1.4 terabytes of disk is attached to this machine. Parallel computations are performed using the message passing interface, MPI (www-unix.mcs.anl.gov/mpi) and through threads using Open MP. We plan to augment the system with an additional 200 Intel Pentium IV class processors in the 2+ Ghz speed grades. Upgrading communication bandwidth to Gigabit Ethernet is also under consideration.

Our goal is to continue to explore the frontier of the commodity component world, as processor, motherboard bus, and memory speeds increase, as fiber cable decreases in price, and as switch speeds increase in performance and decrease in price. We will determine optimal configurations and architectures, within the overall framework of our design. Results from this research will be published and posted on the network, to benefit others seeking a similar price/performance advantage. Similar experiments with regard to disk storage will be conducted.

The Galaxy computer provides computing cycles to CDIC affiliates and projects. Convenient and assured access to local parallel computing is an essential requirement for the development of parallel simulation codes, and it is thus a key component of the CDIC strategy to make state-of-the-art computing technology available to benefit BNL scientific programs.